X-shooter reveals powerful outflows in $z \sim 1.5$ X-ray selected obscured quasi-stellar objects

M. Brusa,[1,2,3]★ A. Bongiorno,[4] G. Cresci,[5] M. Perna,[1,3] A. Marconi,[6] V. Mainieri,[7] R. Maiolino,[8] M. Salvato,[2] E. Lusso,[5,9] P. Santini,[4] A. Comastri,[3] F. Fiore,[4] R. Gilli,[3] F. La Franca,[10] G. Lanzuisi,[1,3] D. Lutz,[2] A. Merloni,[2] M. Mignoli,[3] F. Onori,[10] E. Piconcelli,[4] D. Rosario,[2] C. Vignali[1,3] and G. Zamorani[3]

[1]*Dipartimento di Fisica e Astronomia, Università di Bologna, viale Berti Pichat 6/2, I-40127 Bologna, Italy*
[2]*Max Planck Institut für Extraterrestrische Physik, Giessenbachstrasse 1, D-85748 Garching bei München, Germany*
[3]*INAF – Osservatorio Astronomico di Bologna, via Ranzani 1, I-40127 Bologna, Italy*
[4]*INAF – Osservatorio Astronomico di Roma, via Frascati 33, I-00044 Monte Porzio Catone (RM), Italy*
[5]*INAF – Osservatorio Astronomico di Arcetri, Largo Enrico Fermi 5, I-50125 Firenze, Italy*
[6]*Dipartimento di Astronomia e Scienza dello Spazio, Università degli Studi di Firenze, Largo Enrico Fermi 2, I-50125 Firenze, Italy*
[7]*European Southern Observatory, Karl-Schwarzschild-str. 2, I-85748 Garching bei München, Germany*
[8]*Cavendish Laboratory, University of Cambridge, 19 J. J. Thomson Ave., Cambridge CB3 0HE, UK*
[9]*Max Planck Institut für Astronomie, Königstuhl 17, D-69117 Heidelberg, Germany*
[10]*Dipartimento di Matematica e Fisica, Università degli Studi 'Roma Tre', Via della Vasca Navale 84, I-00146 Roma, Italy*

ABSTRACT

We present X-shooter at Very Large Telescope observations of a sample of 10 luminous, X-ray obscured quasi-stellar objects (QSOs) at $z \sim 1.5$ from the *XMM*-COSMOS survey, expected to be caught in the transitioning phase from starburst to active galactic nucleus (AGN)-dominated systems. The main selection criterion is X-ray detection at bright fluxes ($L_X \gtrsim 10^{44}$ erg s^{-1}) coupled to red optical-to-near-infrared-to-mid-infrared colours. Thanks to its large wavelength coverage, X-shooter allowed us to determine accurate redshifts from the presence of multiple emission lines for five out of six targets for which we had only a photometric redshift estimate, with an 80 per cent success rate, significantly larger than what is observed in similar programs of spectroscopic follow-up of red QSOs. We report the detection of broad and shifted components in the [O III] $\lambda\lambda 5007$, 4959 complexes for six out of eight sources with these lines observable in regions free from strong atmospheric absorptions. The full width at half-maximum (FWHM) associated with the broad components are in the range FWHM $\sim$ 900–1600 km s^{-1}, larger than the average value observed in Sloan Digital Sky Survey type 2 AGN samples at similar observed [O III] luminosity, but comparable to those observed for QSO/ultraluminous infrared galaxies systems for which the presence of kpc scale outflows has been revealed through integral field unit spectroscopy. Although the total outflow energetics (inferred under reasonable assumptions) may be consistent with winds accelerated by stellar processes, we favour an AGN origin for the outflows given the high outflow velocities observed ($v > 1000$ km s^{-1}) and the presence of strong winds also in objects undetected in the far-infrared.

Key words: galaxies: active – galaxies: evolution – quasars: emission lines – quasars: super-massive black holes – cosmology: observations.

1 INTRODUCTION

Since the seminal discovery, 15 yr ago, of the presence of supermassive black holes (SMBHs; $M > 10^6$ M$_\odot$) in the nuclei of virtually all galaxies (Magorrian et al. 1998), it has been realized that active galactic nuclei (AGN) are not exotic phenomena occurring in a small fraction of galaxies, but rather a key ingredient of their formation and evolution.

The 'Soltan argument' (Soltan 1982) posits that most galaxies went through phases of nuclear activity in the past, the remnants

★ E-mail: marcella.brusa3@unibo.it

of which are the quiescent SMBH in $z = 0$ galactic nuclei. During such active phases, a strong physical coupling (generally termed 'feedback') could have established a long-lasting link between hosts and SMBHs, leading to the well-known local scaling relations (e.g. Ferrarese & Merritt 2000; Gebhardt et al. 2000; Gültekin et al. 2009).

While among less luminous sources ($L_{bol} < 10^{45}$ erg s^{-1}), nuclear activity and star formation (SF) can be regulated by local processes such as accretion-triggered gas inflows or disc instabilities likely induced by minor mergers or galaxies encounters (see Ciotti & Ostriker 2007; Bournaud et al. 2011; Cen 2012), among the most luminous sources ($L_{bol} > 10^{46}$ erg s^{-1}), major galaxy mergers are indicated as the culprit for such physical coupling, since they can efficiently funnel a large amount of gas into the nuclear region to feed (and obscure) the accreting SMBH (Menci et al. 2008).

Some AGN-galaxy co-evolutionary models indeed postulate, for the quasi-stellar object (QSO) population, a 'three stages' phase, altogether lasting ≪500 Myr, triggered by the funnelling of a large amount of gas into the nuclear region (e.g. Hopkins et al. 2008; Menci et al. 2008). The first phase (i) is associated with rapid SMBH growth and efficient SF, in a dust-enshrouded, dense environment. Shortly later, (ii) the accreting black hole (BH) should experience the so-called 'feedback' or 'blow-out' phase (see e.g. Hopkins et al. 2008), during which it releases radiative and kinetic energy in the form of powerful, outflowing winds. At this point the accretion on the SMBH is expected to be at its maximum (a blue unabsorbed type 1 AGN or a red obscured type 2 AGN depending on the line of sight through the torus). When the accretion stops, (iii) the galaxy then evolves passively to the massive early-type systems we observe today in local galaxies, with a central quiescent SMBH.

Some key features are common to most model realizations. In particular, powerful winds from all the gas components (neutral, ionized and molecular) are expected in the 'blow-out' phase, and AGN feedback should reveal itself in outflowing material (see King 2010; Fabian 2012 for recent reviews). In addition, the AGN luminosity peak is expected to lag the SF peak: the winds can expel most of the gas in the host galaxy, which is therefore not available anymore to sustain SF and, later, the BH growth, explaining the termination of the two processes. However, differences in the details of the various physical conditions (such as the gas content and consumption time-scales) coupled with different model assumptions (such as time-scale of the processes, fraction of the energy released, lag between SF and AGN activity) translate into the fact that the SF properties of QSOs experiencing the outflow phase may indeed scatter substantially in the different models (see e.g. Lamastra et al. 2013; Hickox et al. 2014). In addition, the degree of obscuration of the QSO is also related to the gas content and depends on the viewing angle with respect to the molecular torus surrounding the accretion disc, the amount of gas available in the host galaxy and the time-scale of the feedback process (see e.g. Martínez-Sansigre et al. 2006).

From an observational point of view, the fact that vigorously star-forming galaxies (e.g. ultraluminous infrared galaxies, ULIRGs) are frequently associated with luminous, often obscured, quasars both in the local Universe and at high-z overall supports a coherent BH–SF growth (e.g. Sanders et al. 1988; Alexander et al. 2005), although at moderate luminosity the coupling is more debated (Harrison et al. 2012a; Mullaney et al. 2012; Page et al. 2012; Rosario et al. 2012). Powerful outflows sustained by relativistic and collimated jets in the hosts of luminous radio galaxies have been commonly observed out to $z \sim 4$ (see e.g. Nesvadba et al. 2008, 2011; Fu

& Stockton 2009). Outflowing winds in radio-quiet objects, most likely to be radiatively driven, are instead less commonly observed. Only very recently spatially resolved optical, far-infrared (FIR) and millimetre spectroscopic studies convincingly showed evidences for the existence of such processes in the form of the predicted energetic outflows in ULIRGs with Seyfert nuclei in the local Universe (e.g. Feruglio et al. 2010; Fischer et al. 2010; Rupke & Veilleux 2011, 2013; Villar-Martín et al. 2011; Zhang et al. 2011; Westmoquette et al. 2012; Rodríguez-Zaurín et al. 2013; McElroy et al. 2014; Harrison et al. 2014; see also Elvis 2000 for a discussion on the ubiquitous presence of winds in the AGN structure).

When moving to higher redshifts ($z > 0.5–1$), several classes of objects (selected on the basis of well-defined observed properties) have been proposed in the recent past as prototype of candidate sources in the outflowing phase. For example, Lípari & Terlevich (2006) first proposed that broad absorption line quasars (BAL QSOs; e.g. Dunn et al. 2010) may be objects in the transition phase between the ULIRGs and unobscured QSO phase, where the outflowing wind in the ionized component is seen directly in optical–ultraviolet (UV) spectra (e.g. de Kool et al. 2001; Hamann et al. 2002). Extensive works in the past years uniquely contributed to our understanding of the winds physics, in terms of spatial location, ionization level and energetics involved (see e.g. Moe et al. 2009; Arav et al. 2013; Borguet et al. 2013). Recent works also suggest that ~40 per cent of infrared (IR) selected and Sloan Digital Sky Survey (SDSS) QSOs are BAL QSOs, pointing towards the fact that they are quite common (Dai, Shankar & Sivakoff 2008; Allen et al. 2011) and that the outflow and unobscured phases may be of comparable length, in agreement with the Hopkins scenario (see also Glikman et al. 2012). Moreover, from the analysis of [O III] luminosity matched obscured and unobscured samples of QSOs at $z \sim 0.5$ presented in Liu et al. (2013) and Liu, Zakamska & Greene (2014), it has been proposed that high luminosities ($L[O III] > 10^{43}$ erg s^{-1}) are characteristic of the peak of quasar feedback phase.

Given that the sources in the feedback phase are expected to be dusty and reddened (either by the host galaxy or the torus), another class of objects proposed to be in the transition phase are the 'red QSOs', selected from large area, bright IR surveys such as Two Micron All Sky Survey (2MASS) or UKIRT Infrared Deep Sky Survey (UKIDSS), on the basis of a red colour in the near-infrared (NIR) band (e.g. $J − K \gtrsim 2$) indicative of a steep spectral energy distribution (SED) due to obscured AGN (Urrutia et al. 2009; Banerji et al. 2012; Glikman et al. 2012). Detailed high-resolution imaging, spectroscopy or morphological follow-up of carefully selected prototypes of this class of sources at various redshifts convincingly favour such an interpretation (e.g. Urrutia et al. 2012; Banerji, Fabian & McMahon 2014). Finally, another well-studied class of objects are the submillimetre galaxies (SMG) associated with ULIRGs and luminous QSOs mentioned above. Only recently, with the advent of high resolution and sensitive NIR spectrographs, it has been possible to break the $z > 1$ barrier and characterize the neutral and ionized kinematic components of luminous high-z quasars by sampling the redshifted optical lines in the NIR band (e.g. Alexander et al. 2010; Cano-Díaz et al. 2012; Harrison et al. 2012b, hereafter H12; Maiolino et al. 2012).

Luminous X-ray selected obscured AGN with red colours also represent optimal targets for objects where feedback from the AGN is expected to halt SF and to start 'cleaning' out gas from the galaxy. Indeed, in the AGN evolutionary framework described above, the obscured phase of a quasar corresponds to a time when the BH is accreting mass very rapidly, implying that the SMBH should

manifest itself as an X-ray quasar. In this respect, while most if not all of the studies at $z > 1$ have been performed on QSO/ULIRGs and objects undergoing intense SF, a selection based on the X-ray emission offers the advantage of being independent of the SF properties, which as mentioned above cannot be predicted a priori for the QSOs in the feedback phase. In a previous work based on *XMM–Newton* observations of the Cosmic Evolution Survey (COSMOS) field (Scoville et al. 2007) we proposed a criterion to isolate such very rare objects, on the basis of their observed red colours and high X-ray to optical and/or mid-infrared (MIR) to optical flux ratios (Brusa et al. 2010, hereafter B10). The combined analysis of a high-resolution Keck spectrum, morphology from *Hubble Space Telescope* (*HST*)/Advanced Camera for Surveys (ACS) data and an accurate SED fitting of the prototype of this class of sources (XID 2028) convincingly showed that the proposed criteria appear robust in selecting luminous and obscured quasars in the 'blow-out' phase discussed above (see section 9 in B10). In this paper we present the data reduction and analysis of X-shooter observations at the Very Large Telescope (VLT) of the 10 brightest obscured QSOs at $z \sim 1.5$ in the *XMM*-COSMOS survey, and we will focus on the detection of the broad and shifted components in [O III] lines. The measurement of the BH masses from the same data is presented in a companion paper (Bongiorno et al. 2014).

The paper is organized as follows: Section 2 presents the sample selection and properties, Section 3 the X-shooter observations and data reduction and Section 4 the data analysis and the results of the spectral fitting. Section 5 discusses the main result, i.e. the origin of the broad component and the outflows statistics. Section 6 discusses the energetic output associated with the outflow and finally we summarize our results and the implications in Section 7. In Appendix A we present the fit of the Urrutia et al. (2012) sample. All the rest-frame wavelengths are given in the air, as quoted in http://www.sdss3.org/dr8/spectro/spectra.php. Unless otherwise stated, uncertainties are quoted at the 68 per cent (1σ) confidence level. Throughout the paper, we adopt the cosmological parameters $H_0 = 70 \text{ km s}^{-1} \text{ Mpc}^{-1}$, $\Omega_m = 0.3$ and $\Omega_\Lambda = 0.7$ (Spergel et al. 2003). In quoting magnitudes, the AB system will be used, unless otherwise stated.

2 SAMPLE SELECTION AND LUMINOUS OBSCURED QSOs PROPERTIES

2.1 Sample selection

The *XMM*-COSMOS survey (Hasinger et al. 2007; Cappelluti et al. 2009) consists of $\sim$1800 X-ray AGN selected over the entire 2 deg^2 COSMOS field, with complete multiwavelength data from radio to UV, including spectroscopic and photometric redshifts, as well as morphological classification, accurate estimates of stellar masses, star formation rate (SFR) and IR luminosities (see B10; Salvato et al. 2011; Bongiorno et al. 2012; Lusso et al. 2012; Rosario et al. 2012; Santini et al. 2012). In particular, the *XMM*-COSMOS survey has the combination of area and depth necessary to sample with the adequate statistics rare objects (such as those expected in the 'feedback' phase discussed above) otherwise missed in pencil-beam surveys such as the *Chandra Deep Fields* (see e.g. Alexander & Hickox 2012 for a review). In addition, the *XMM*-COSMOS survey sample obscured objects at lower intrinsic luminosity ($L_{bol} \sim 10^{45-46.5} \text{ erg s}^{-1}$) than the 'monsters' accessible from larger area IR surveys [e.g. *Wide-field Infrared Survey Explorer* (*WISE*) targets, $L_{bol} > 10^{47}$; Weedman et al. 2012; see also Banerji et al. 2012], more representative of the entire luminous QSO population.

In B10 we presented a sample of $\sim$170 obscured AGN isolated from the entire *XMM*-COSMOS sample, on the basis of their observed-frame mid-infrared (flux$_{24\,\mu m}$/O $>$ 1000), near-infrared ($R - K > 5$ or $R - [3.6] > 4$), optical and X-ray (X/O $>$ 10) properties (following Fiore et al. 2003, 2009; Mignoli et al. 2004; Brusa et al. 2005, Melini et al., in preparation). We made use of the spectroscopic information and of the availability of spectral classifications, to assess the reliability of colour cuts and flux ratios as diagnostics of the presence of obscured sources: of the 20 sources with optical spectra available, the vast majority (80 per cent) are classified as narrow line (NL) AGN, and most of them are X-ray obscured ($\langle$HR$\rangle \sim -0.2$, HR being defined as $(H - S)/(H + S)$, where H and S are the counts in the 2–10 and 0.5–2 keV bands, respectively). The adopted criteria appear therefore robust in selecting additional $\sim$150 X-ray obscured objects lacking broad lines (BLs) in the optical spectrum in the redshift range $z \sim 1$–3. In Fig. 1 we plot the selection regions in the two diagnostics described above that we used to select our X-shooter targets; the small empty circles in this plot represent the full *XMM*-COSMOS population.

From the original sample of $\sim$170 objects, we selected all the sources with $K < 19$ and deabsorbed rest frame $F_{2\text{-}10} > 5 \times 10^{-15} \text{ erg cm}^{-2} \text{ s}^{-1}$. We then extracted all the sources with photometric redshifts in the range $z = 1.25$–1.72 (i.e. those for which Hα and [O III] lines are expected to lie in regions free from strong atmospheric absorptions). This sums up to a total of 12 objects we proposed for our X-shooter observations, of which 10 were observed (see Section 3). The 10 targets comprise: three spectroscopically confirmed obscured AGN (XID 2028, XID 60053, XID 5053) selected on the basis of the lack of broad emission lines (C IV, Mg II) in the optical spectra, one BL AGN (XID 18) and six objects with only photometric redshifts. In Fig. 1 objects marked with large symbols are those with redshift in the range $z = 1.25$–1.72 and satisfying the conditions on the K band and the X-ray flux: blue circles denote spectroscopically confirmed BL AGN, red circles spectroscopically confirmed NL AGN and cyan triangles objects with only photometric redshifts. The yellow circles are the obscured AGN candidates observed by X-shooter, e.g. sources which satisfy one ($R - K > 5$ and X/O $>$10) or the other ($\log(\nu_{24}F_{24}/\nu_R F_R > 1$ and $R - [3.6] > 4$) selection criterion.

Our sample is similar in size, but more homogeneous in the selection, with respect to the sample presented in H12 (10 objects), which represents one of the most recent analysis and study of [O III] profiles in high-z ($z \sim 2$) SMG/AGN systems. The sample is also similar in size to the sample of heavily reddened quasars at $z \sim 2$ selected from the UKIDSS Large Area Survey (ULAS; Banerji et al. 2012; 12 objects). We note that, although our sources on average show a lower/bluer $J - K$ colour ($(J - K)_{Vega} \sim 1.5$–2.5 likely due to the on average lower redshift of the objects) than the colour cut used in Banerji et al. (2012) ($J - K > 2.5$), they actually populate the same region of the $I - K$ versus I-band diagnostic, extending to faint magnitudes given the deeper limiting fluxes of COSMOS with respect to ULAS. Indeed, our prototype source (XID 2028) is selected as a red quasar from ULAS (ULAS J1002+0137) and a Spectrograph for Integral Field Observation in the Near-Infrared (SINFONI) spectrum is presented in Banerji et al. (2012).

The most important properties of the targets are reported in Table 1, and discussed below in detail. The multiwavelength properties, including the fluxes measured in the selection bands, can be retrieved via the XID from the B10 catalogue publicly available at http://www2011.mpe.mpg.de/XMMCosmos/xmm53_release/.
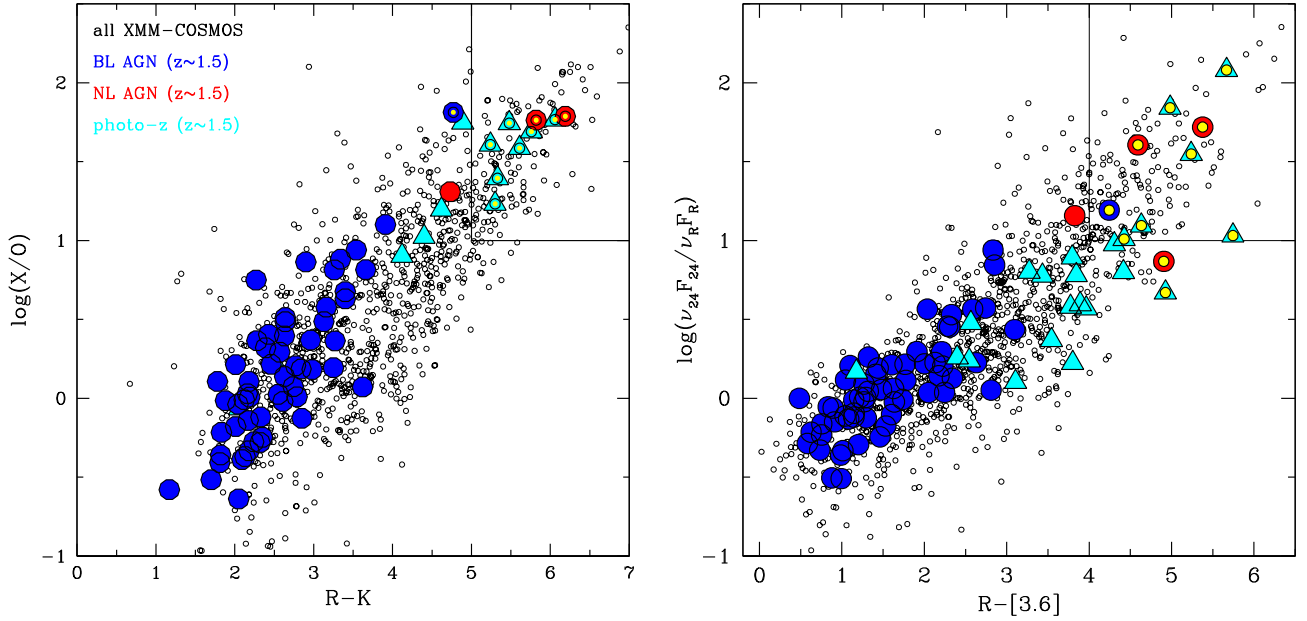
Figure 1. Selection region for the X-shooter targets. (a) X-ray to optical flux ratio versus $R - K$ (Vega) colour and (b) 24 μm to optical flux ratio versus $R - [3.6]$ colour for all the *XMM*-COSMOS sources (small empty circles) and for those with redshift in the range $z = 1.25$–1.72, $K < 19$ and $F_{2\text{-}10,\text{rest}} > 5 \times 10^{-15}$ erg cm^{-2} s^{-1} (large symbols). Blue circles denote spectroscopically confirmed BL AGN, red circles spectroscopically confirmed NL AGN and cyan triangles objects with only photometric redshifts. The yellow circles are the obscured AGN candidates proposed for the X-shooter observations, e.g. sources with photometric redshifts which satisfy one ($R - K > 4.5$ and X/O >10) or the other ($\log(\nu_{24}F_{24}/\nu_R F_R > 1$ and $R - [3.6] > 4$) selection criterion.

Table 1. Main accretion and hosts galaxies properties for our 10 X-shooter targets.

XID (1)	RA (^{h}:^{m}:^{s}) (2)	Dec. ($^\circ$:$'$:$''$) (3)	z (4)	$\log(L_X)$ (erg s^{-1}) (5)	$\log(N_H)$ (cm^{-2}) (6)	$\log(M_*)$ (M$_\odot$) (7)	$\log(M_{BH})$ (M$_\odot$) (8)	SFR (M$_\odot$ yr^{-1}) (9)	$S_{1.4\,\text{GHz}}$ (μJy) (10)	$\log(L_{AGN})$ (erg s^{-1}) (11)	L/L_{Edd} (12)	Spec z (13)
18	10:00:31.93	02:18:11.8	1.598	44.9	22.5	11.39	8.68	4.9	<80	46.2	0.5	1.6073
60053	10:01:09.25	02:22:54.7	1.582	>43.5†	**	11.17	8.65	740*	718	46.1	1.0	1.5812
175	09:58:52.97	02:20:56.4	1.55(p)	44.7	21.4	11.55	9.44	1.4	<80	45.6	0.10	1.5297
2028	10:02:11.27	01:37:06.6	1.592	45.3	21.9	11.92	9.44	275*	102	46.3	0.05	1.5927
5321	10:03:08.83	02:09:03.5	1.27(p)	45.7	21.6	12.22	9.81	230*	180	46.3	0.01	1.4702
5053	10:01:29.03	01:57:11.6	1.374	44.3	23.2	11.03	–	<1	<80	45.3	–	1.3735
5325	10:02:18.83	02:46:04.3	1.43(p)	43.1	20.0	11.19	7.50	28.8	<80	44.6^a	1.0	1.3809
5573	09:58:07.15	01:47:08.5	1.66(p)	44.4	22.2	10.91	–	16.5	<80	45.1	–	1.1152
54466	10:02:25.34	02:26:14.1	1.47(p)	43.8†	23.2	10.93	–	107*	191	45.2	–	1.0034
31357	10:01:34.97	02:38:07.3	1.71(p)	44.5	23.2	11.24	–	<1	<80	45.3	–	–

Notes. The first five sources in the upper part are those with BH masses measurements presented in Bongiorno et al. (2014). Column (1): XID from B10; columns (2) and (3): optical coordinates (J2000); column (4): redshift available before the X-shooter run, (p) marks photometric redshift; columns (5) and (6): X-ray luminosities (L_X, unobscured) and column densities are in the 0.5–10 keV rest frame range and they are obtained from proper spectral analysis if available (Mainieri et al. 2011) or from rest-frame flux corrected from absorption as inferred from the HR (sources marked with †, following Merloni et al. 2014), the source marked with a double asterisks (**) is a candidate Compton thick AGN; column (7): stellar masses are from Bongiorno et al. (2014, first five sources) or Bongiorno et al. (2012, last five sources), computed from SED fitting and assuming a Chabrier IMF; column (8): BH masses from Bongiorno et al. (2014); column (9): SFR are from Bongiorno et al. (2012) or Bongiorno et al. (2014), sources marked with an asterisk (*) are those with detection in PEP; column (10): the 1.4 GHz flux is taken from the VLA survey of COSMOS (Schinnerer et al. 2010); column (11): bolometric luminosity from SED fitting as derived from Lusso et al. (2012), for the source marked with ^{a}, L_{bol} is derived from L_X and a $k_{bol} \sim 20$; column (12): Eddington ratio; column (13): redshift as measured in this work.

2.2 Host galaxies properties

For all the targets, host galaxies stellar masses (M_*) and SFR based on galaxy and AGN decomposition are already available[1] (Bongiorno et al. 2012, 2014). Four of the targets (XID 5321, XID 2028,

XID 60053 and XID 54466) are detected in the PACS Evolutionary Probe (PEP) survey by *Herschel*/Photodetector Array Camera and Spectrometer (PACS) in at least one band (Lutz et al. 2011; Santini et al. 2012). For these objects, L(FIR, 8–1000 μm) were estimated by fitting monochromatic PACS fluxes with Dale & Helou (2002) IR templates, using the same technique as in Santini et al. (2009), and the luminosity was then converted into a SFR using the relation from Kennicutt (1998), assuming a Chabrier initial mass function (IMF).

---

[1] For those sources for which we could provide a new spectroscopic redshift (see Section 4.1), we re-run the code and recomputed M_* and SFR.

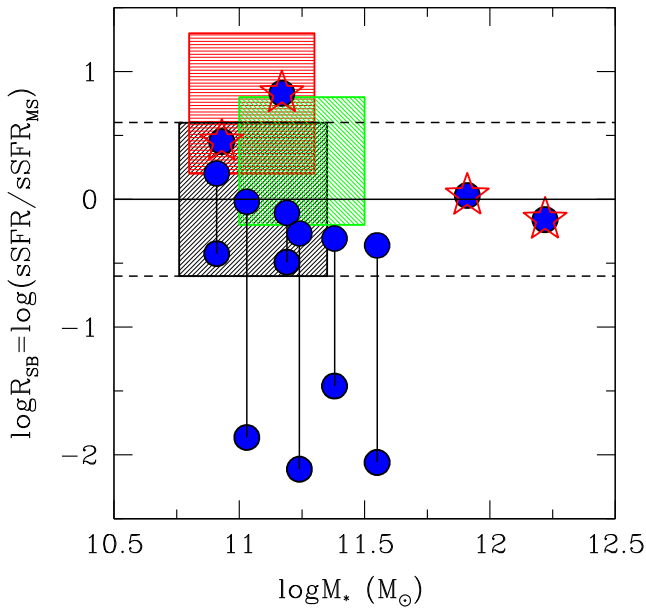**Figure 2.** Ratio between the specific star formation rates (sSFR = SFR/M_*) of our targets with respect to those expected for main-sequence galaxies (sSFR$_{MS}$) at a given stellar mass, versus the host stellar mass M_*. The ratio R_{SB} = sSFR/sSFR$_{MS}$ is plotted in logarithmic scale. The sSFR values are normalized assuming the best fit of the galaxy main sequence as a function of redshift obtained by Whitaker et al. (2012). The dashed horizontal lines mark the region of MS galaxies. Starred symbols mark objects for which the SFR is derived from PACS photometry. For the six sources undetected in PEP, we report as blue circles the value corresponding to the SFR derived from the SED fitting decomposition (lower paired points), and the R_{SB} value computed assuming a SFR ∼ 70 M$_\odot$ yr^{-1} as derived from stacking of the PACS fluxes (upper paired points; see text for details). The shaded areas mark the loci occupied by the $z \sim 2$ SMG/ULIRGs presented in H12 (red), the eight massive star-forming galaxies presented in Förster Schreiber et al. (2014) (green) and the MS galaxies presented in Kashino et al. (2013) (black).

All our targets have M_* in the range 10^{11}–10^{12} M$_\odot$. The SFR and stellar mass properties of our targets are shown in Fig. 2, where we plot the 'starburstiness' R_{SB} = sSFR/sSFR$_{MS}$ of the host galaxies versus M_*. The specific star formation rate (sSFR = SFR/M_*) of our targets is normalized assuming the best fit of the galaxy main-sequence (MS) as a function of redshift obtained by Whitaker et al. (2012). Our targets are marked by blue symbols; those detected in the PEP survey have been highlighted by a red star. From this figure it is possible to see that, with the exception of XID 60053 which is above the MS, our targets lie in or below the MS of star-forming galaxies at $z \sim 1.5$ as defined by the black line (Whitaker et al. 2012). For the six PEP undetected sources, we report in Fig. 2 two values of R_{SB} (paired by solid lines): the lower one is obtained using the SFR obtained from SED fitting while the upper one is plotted assuming a SFR ∼ 70 M$_\odot$ yr^{-1}, corresponding to the PEP stacked signal detected at ∼3σ level. Even if the SFR from SED fitting were severely underestimated, the PEP stacked signal confirms that these systems are not actively forming stars with respect to their stellar mass. In particular, the four objects with SFR from SED fitting <10 M$_\odot$ yr^{-1} (logR_{SB} < −1) may be in their way to be quenched (see also Mignoli et al. 2004; Mainieri et al. 2011). In contrast, the SMG/ULIRG sample presented in H12 is on average above the MS of star-forming galaxies at the same redshift ($z \sim 2.2$; see red shaded area in Fig. 2). In the same plot we also show the

loci occupied by two other samples we will use in the following as comparison: the green area marks the locus occupied by the eight massive star-forming galaxies presented in Förster Schreiber et al. (2014), while the black area marks the mass range of MS star-forming galaxies presented in Kashino et al. (2013).

Differently from H12, for which a radio detection was imposed to conduct the integral field unit (IFU) follow-up, only 40 per cent of our objects (all those detected also in PACS) are detected in the radio band at 1.4 GHz in the Very Large Array (VLA) observations of the COSMOS field (Schinnerer et al. 2010). The radio power implied by the detections in the survey ($L_{1.4\,GHz} = 10^{23}$–10^{24} W Hz^{-1}) places these objects below the radio-loud class, and they are also one order of magnitude fainter than the high-z radio galaxies and the SMG/ULIRGs discussed in H12 (see their fig. 1b). In particular, the low level of radio emission (apart from 60053) assures little or marginal contribution from radio jets in the energetic of the systems.

Fig. 3 shows the *HST*/ACS cut-outs of the nine sources for which *HST* data are available, with overplotted the slits positions and widths. The morphology of our prototype object (XID 2028, bottom left in Fig. 3) was already presented in B10 (see their fig. 13). A clear point-like nucleus is present associated with an extended, asymmetric emission. Similarly, XID 175, XID 54466, XID 5573, XID 5325 and XID 18 present point-like nucleus likely responsible for the X-ray emission, as well as residual diffuse or patchy components and/or close companions, which may trace the host galaxy, extending on scales comparable to or even larger than the slits apertures (∼8 kpc, see next section). Of the remaining three, XID 60053 is a patchy irregular galaxy, XID 31357 is an elongated, likely edge-on disc galaxy, while XID 5053 may be an elliptical galaxy, consistent with the very low SFR derived from the SED fitting. XID 5321, unfortunately, lies outside the *HST*/ACS coverage of the COSMOS field. For this source we show in Fig. 4 the ground-based image with the best resolution available in the COSMOS, i.e. the *J*-band UltraVista image. The diameter of the source corresponds to scales of ∼30 × 40 kpc at $z = 1.47$. This is our X-ray brightest ($L_X = 5$–10^{45} erg s^{-1}) and most massive ($M_* \sim 10^{12}$ M$_\odot$) target, with a total IR luminosity (AGN+SF) of the order of $L > 10^{47}$ erg s^{-1}, similar to those discovered in the IR surveys (*WISE*; Banerji et al. 2012; Weedman et al. 2012).

2.3 Accretion properties

Rest frame, absorption corrected X-ray luminosities in the 0.5–10 keV band (L_X) and absorbing column densities (N_H) have been obtained from proper spectral analysis for objects with enough counting statistics (>150 counts; Mainieri et al. 2011). For the objects with low counting statistics, the N_H is inferred from the observed hardness ratio and it is used to *K*-correct the rest-frame flux to derive the unobscured luminosity (see Merloni et al. 2014). Most of our sources have $L_X > 10^{44}$ erg s^{-1} and moderate to large obscuring column densities ($N_H > 10^{21}$ cm^{-2}). We note that the N_H measured are based on relatively low counts data that cannot disentangle the complexity of the spectra and different components. In particular, the multiwavelength analysis of XID 60053 suggests that for this source the column density is heavily underestimated (and therefore the unobscured L_X) and this object is a candidate Compton thick (CT) AGN (see Bongiorno et al. 2014).

We estimated the total AGN bolometric luminosities (L_{bol}) for our sources following the methods presented in Lusso et al. (2012, 2013) for the *XMM*-COSMOS sample. More in detail, the L_{bol} associated with the AGN component has been evaluated from SED fitting decomposition of the galaxy, torus and SF components, and has been
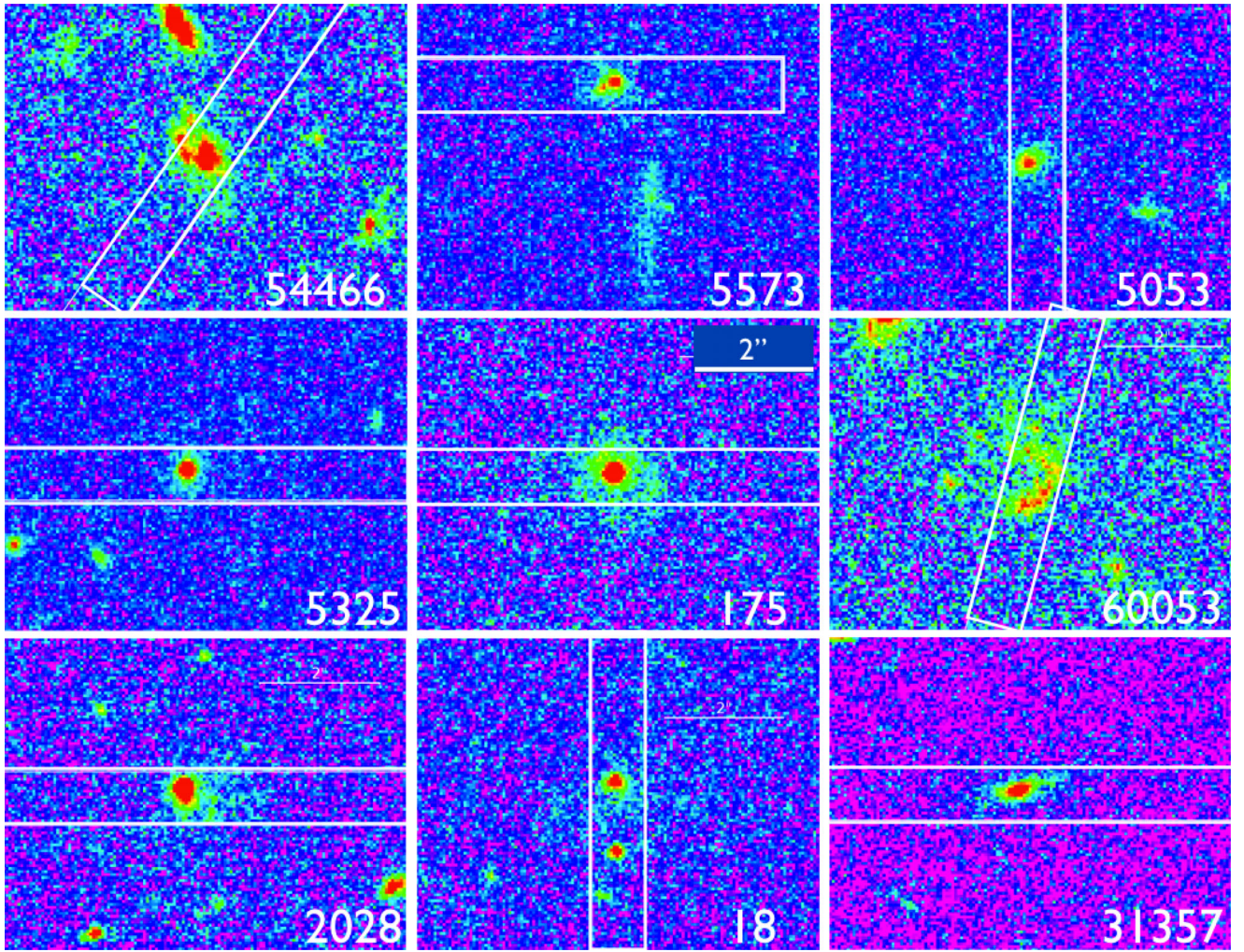
Figure 3. I_{814}-band cut-outs around the nine targets with *HST*/ACS data (all but XID 5321 which lies outside the *HST* COSMOS area), ordered by increasing redshifts (same as Fig. 5). The labels indicate the XID. In the central panel we report also the 2 arcsec scale ($\sim$17 kpc at $z \sim 1.5$) common to all the figures, and the 0.9×11 arcsec^2 slit used in the X-shooter observations is marked in each panel. The intensity level of the images is logarithmic, with blue/purple marking the background level and red marking the peak emission, with an average contrast of about a factor of 10.

Figure 4. UltraVista *J*-band cut-out for source XID 5321, the only one lacking *HST*/ACS data. The 2.5 arcsec scale is shown on the bottom left, as well as the 0.9×11 arcsec^2 slit and position used for the NIR observations.

derived by integrating the torus component only for type 2 AGN or from the combined constraints from the disc and torus emission for type 1 AGN. Overall, our targets have total AGN luminosities in the range $L_{bol} = 10^{45-46.5}$ erg s^{-1}, with median value $L_{bol} = 10^{46}$ erg s^{-1}. When comparing the X-ray and the bolometric AGN luminosities, we note that these sources have bolometric corrections in the range $k_{bol} = L_{bol}/L_X \sim 4-20$, lower than the value generally assumed for optically selected samples ($k_{bol} \sim 20-30$; e.g. H12; see discussion in Lusso et al. 2012).

Finally, Bongiorno et al. (2014) published the BH masses measured from the X-shooter data for five out of 10 of our targets. XID 5325 was not included in Bongiorno et al. (2014) because of its low N_H value ($<10^{21}$ cm^{-2}). However, a broad component is detected in the Hα line (see Section 4.2) and it is possible to derive a BH mass following the same calibration presented in Bongiorno et al. (2014). From the comparison between L_{bol} and the Eddington luminosity associated with the measured M_{BH}, it is possible to infer also the Eddington ratios (L/L_E) for these six sources, in the range $L/L_{Edd} = 0.01-1$ (see Table 1). The source accreting at the Eddington level is XID 60053, the candidate CT AGN.

3 OBSERVATIONS AND DATA REDUCTION

The *XMM*-COSMOS obscured QSOs targets have been observed with the X-shooter spectrograph (D'Odorico et al. 2006; Vernet et al. 2011) on the ESO VLT-UT2 (Kueyen) during the nights of 2013 February 8–10 as part of programme 090.A-0830(A). Because of scheduling constraints and time losses during the visitor mode run (see below), only 10 targets have been observed.

X-shooter is an echelle spectrograph, with UV, visible and NIR channels providing nearly continuous spectroscopy from 0.3 to 2.48 μm. Given the nature of our sources (very red and optically obscured, with $R - K > 5$), although all the sources were observed with all three arms (UVB, VIS and NIR), they returned signal only in the NIR arm (all targets) and in the VIS arm (with clear continuum and/or [O II] λ3727 detection in all but one targets). All the targets were acquired with acquisition images of 30–120 s, and with a blind offset from a United States Naval Observatory (USNO) bright star. Ad hoc position angles were set for all the sources in order to maximize the efficiency of the observations (e.g. trying to remove contaminants in the slit if at positions not suitable for the dithering; see slits position superimposed in Figs 3 and 4).

The exposure times range from 1 to 2 h. We used the 0.9 arcsec width slit (corresponding to a spectral resolution $R \sim 5100$ in the NIR and $R \sim 8800$ in the VIS). In the NIR arm we adopted the *JH* filter (with the *K*-band filter blocked): this solution reduced the background in the *J* band, essential for our faint targets. In the NIR we dithered 600 s observations[2] in an ABBAAB sequence (e.g. for a 1 h observation) at positions +2.5 and −2.5 arcsec from the central coordinates along the slit long axis. Observing conditions were reported to be photometric, and seeing condition was 0.5–1.0 arcsec (FWHM). We base our flux calibration on observations of the standard stars LTT 3218 and GD 71 taken during the three nights with the same photometric conditions and seeing. For most targets, a telluric standard of type B8V–B9.5V was observed before and after our primary target, in order to create a telluric absorption spectrum at the same airmass as the observations of our targets and to flux calibrate the data.

The data reduction of the three separate arms has been done with REFLEX (Freudling et al. 2013). Previous versions of REFLEX pipeline reported known problems with observations obtained with the *JH* blocking filter and flux calibration in the NIR arm. These problems have been corrected in the newest version (v2.4). We carefully checked the full data reduction and flux calibration obtained with REFLEX v2.4 in the NIR arm by re-reducing manually with ESOREX and the X-shooter recipes the standard stars observed in the three nights. Results on flux calibration were consistent within 10 per cent, and we therefore we adopted the response matrix obtained from the pipeline products. The X-shooter pipeline gives as an output the wavelength solution measured in air, and we will refer to this system when measuring redshifts. From the wavelength and flux calibrated 2D spectra, we manually extracted the 1D spectrum optimizing the extraction region (position along the slit and aperture) with the ESOREX task XSH_SCIRED_SLIT_NOD. All the spectra have been extracted from an aperture of $\sim$1 arcsec, corresponding to physical sizes $\sim$8 kpc.

Fig. 5 shows the 10 X-shooter VIS+NIR spectra of our *XMM*-COSMOS targets, sorted by increasing redshift (as determined in Section 4.1). The shaded areas in each spectrum mark the regions of

the Hβ+[O III] (left) and Hα+[N II] (right) lines. The flux calibration of the two arms has been done with the same standard star and the two spectra (VIS and NIR) for each target show an excellent match in absolute flux in the overlapping regions (few tens of Å).

4 RESULTS

4.1 Spectroscopic redshifts

We chose as best fitting solution for the spectroscopic redshift the one which produces the best fit to the wavelengths of the narrow components of the [O III] $\lambda\lambda$4959, 5007, [N II] $\lambda\lambda$6548, 6581 and Hα lines (see next section). We used these observed wavelengths to compute the systemic redshift. For the objects with significant signal in the VIS spectrum, we also imposed the solution to be consistent with the position of the resolved doublet of the [O II] line ($\lambda\lambda$3726.0, 3728.8 Å).[3]

Fig. 6 shows a zoom of the Hβ+[O III] (left) and Hα+[N II] (right) regions for the nine sources for which we could assign accurate redshifts. Each row corresponds to a different object, and in each panel we show the extracted spectrum (centre), along with the corresponding 2D spectrum (upper inset). The observed frame wavelengths and the aperture used to extract the spectrum are also shown on the 2D image. The proposed redshift solution is labelled in the left-hand panel, and the corresponding wavelengths of Hβ, [O III] $\lambda\lambda$4959, 500 (left-hand panel) and [N II] λ6548, Hα, [N II] λ6581 and [S II] $\lambda\lambda$6720, 6735 (right-hand panel) are superimposed on the 1D spectra. Two sources have only the Hα line (XID 54466) or the [O III] lines (XID 5573) in a good portion of the spectrum. For these two objects the redshift solution has been determined using only the accessible lines and they are shown on the same (last) row of Fig. 6. Finally, for XID 31357, due to the low signal-to-noise (S/N) of the spectrum, the identification is less secure and only tentative. We note that the excess clearly visible in the NIR spectrum at just below 1.3 μm (see Fig. 5, lower panel) may be real, but cannot be identified as the [O III] line, given that the Hα then should appear at $\lambda \sim 1.65$ μm in a region free from strong atmospheric absorptions.

Overall, we were able to confirm the redshift of the four objects with optical spectra already available, and to assign new spectroscopic redshifts to five out of six sources. Two of the five objects with photometric redshifts for which we were able to assign a spectroscopic redshifts (XID 5573, XID 54466) have $\Delta z/(1 + z_{\rm spec}) > 0.2$, considerably larger than the current precision ($\sigma_{\Delta z/(1+z_{\rm spec})} \sim 0.015$) to which photo-$z$ for AGN have been computed for the *XMM*-COSMOS sample (see Salvato et al. 2011). Photometric redshifts via SED fitting are always calibrated on the basis of a spectroscopic sample. This is true in particular for AGN where the relative galaxy/AGN contribution is unknown and the libraries of templates change, depending on the type of sources we want to fit (Salvato et al. 2011). The two sources with $\Delta z/(1 + z_{\rm spec}) > 0.2$ are fainter than the objects used for the spectroscopic training sample for the

---

[2] In the VIS and UVB arm we dithered the observations in the same way, but we reduced the exposure times of each frame to 563 and 525 s, respectively, in order to gain in efficiency during the readout time for each object.
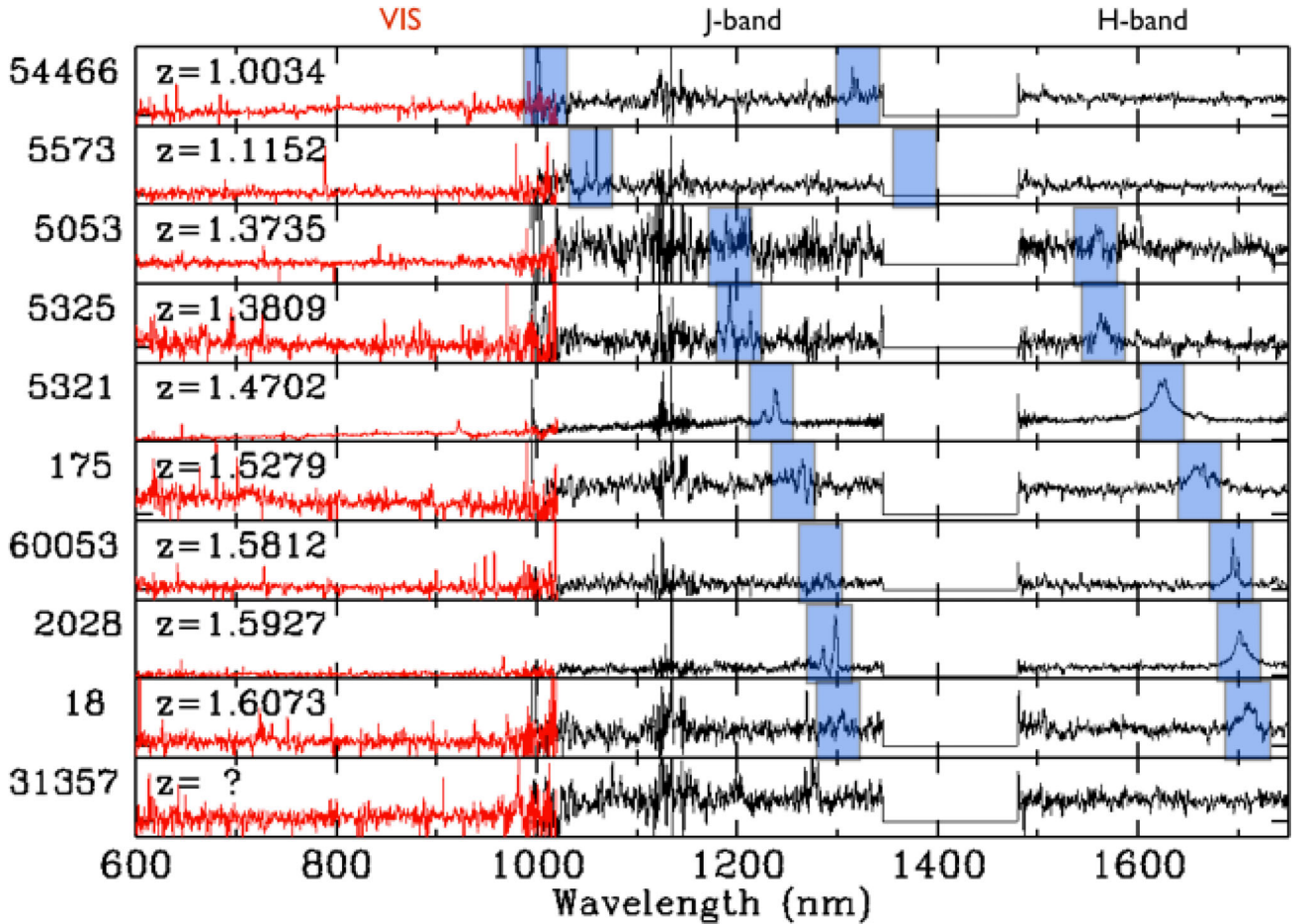
[3] Vernet et al. (2011) quote a wavelength calibration accuracy of the order of 2 km s^{-1} in the VIS arm and 4 km s^{-1} in the NIR arm. We checked the wavelength calibration in our reduced spectra with the positions of known sky lines in the optical (e.g. $\lambda\lambda$5577.32, 6300.30 Å, from Gindilis & Pariiskii 1961, http://www.star.ucl.ac.uk/m~sw/lines.html) and in the IR (from the table given in Rousselot et al. 2000) and they agree within 10 km s^{-1}. This is well below the resolution of the instrument in both arms ($\sim$40 and $\sim$60 km s^{-1}, respectively) and results in a internal velocity accuracy of the order of $\Delta z = 0.0004$.

Figure 5. X-shooter NIR spectra (black) of the 10 *XMM*-COSMOS targets sorted by increasing redshift. The XID and redshifts of the sources are given on the left of each panel. The range from ~1 up to 1.75 μm is shown for the NIR spectrum. The bad region (due to low atmospheric transmission) defining the limits between the *J* and *H* filters is masked out. The shaded areas in each spectrum mark the wavelengths ranges of the redshifted [O III] (left) and Hα (right) lines. Zoom of these regions are given in Fig. 6. The VIS spectra are also shown in red in the 6000 Å–1 μm range. The fluxes are all flux calibrated in erg cm^{-2} s^{-1} Å^{-1}, but the scale is not shown on the *y*-axis.

XMM-COSMOS AGN and therefore the discrepancy is not surprising. This discrepancy also caused the two targets to be the only two lacking information on both Hα and [O III] line complexes.

The success rate in assigning secure spectroscopic redshifts to colour-selected objects (5/6, ~83 per cent) is higher than that reported in similar programs of spectroscopic follow-up of red quasars: for example, Banerji et al. (2012) were able to assign secure redshifts to five out of 13 objects (~40 per cent) in their SINFONI *H*+*K* follow-up of red quasars (see also Sarria et al. 2010; Bongiorno et al. 2014). Our higher spectroscopic success rate can be mainly ascribed to the larger X-shooter range covering both the visible and the entire NIR bands, down to the *J* filter. Indeed, the two sources with $\Delta z/(1 + z_{spec}) > 0.2$ mentioned above have spectroscopic redshifts $z = 1–1.2$ and therefore Hα is not sampled in the SINFONI *H* and/or *K* band used in the mentioned programs. Had these sources been observed with only the *H* or *K*-band filters (or both) they would have turned out to be featureless, dropping the success rate to 50 per cent. In addition, Banerji et al. (2012) speculate that the objects for which they could not derive redshifts are ruminous red galaxies at $z < 1$, and therefore they do not show any feature in the NIR bands. The selection on the basis of the X-ray emission of our targets assures a negligible contamination by LRG despite the similar optical to IR colours.

4.2 Modelling the Hβ + [O III] and Hα + [N II] line complexes

To determine the dynamics and the outflow properties from the [O III] line profile fitting, we proceeded as follows. First, we brought all the spectra to the rest frame by dividing the wavelength by $(1 + z)$. The rest-frame wavelengths are reported in the lower *x*-axis in each panel of Fig 6. In doing so we also multiplied the flux by $(1 + z)$ in order to conserve the observed integrated flux in the rest-frame fit. Prior to the modelling of the emission line profiles, the continuum was subtracted. We estimated the local continuum by fitting a power law to the spectra at both sides of the two regions (Hβ+[O III], Hα+[N II]) using those wavelength ranges that are not affected by prominent emission or absorption features (e.g. 4200–4300 and 5050–5200 Å for the [O III] lines).

Once the continuum has been subtracted, for all our nine targets we fit the two regions with three sets[4] of Gaussian profiles:

Set 1: (systemic, 'S'): eight Gaussian lines, one for each emission line (namely: Hα and Hβ, and the [O III], [N II] and [S II]

---

[4] For sources with only the Hβ+[O III] (XID 5573) or Hα+[N II] (XID 54466) lines in a good portion of the spectrum we modified the set of Gaussians accordingly.
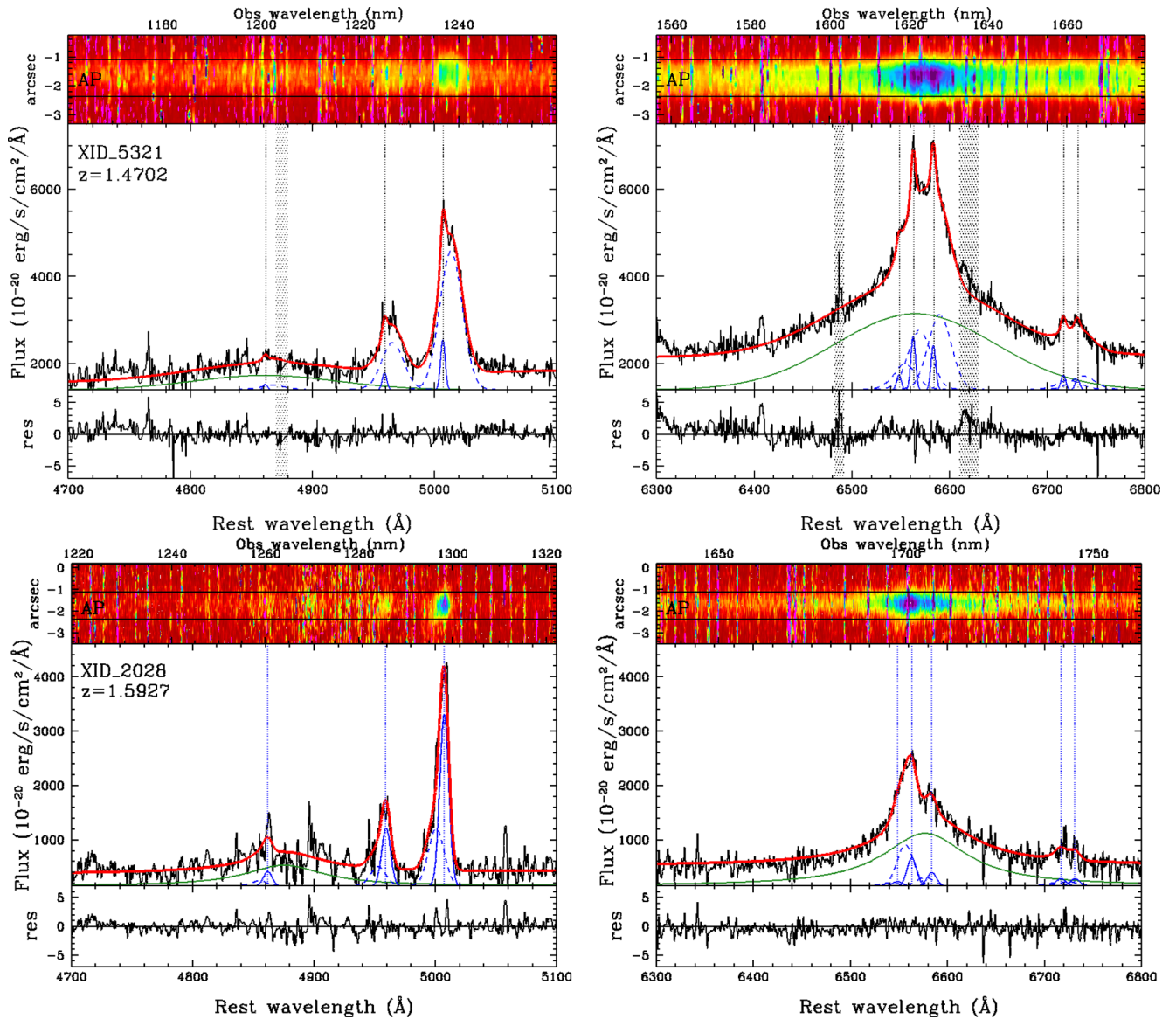
Figure 6. Zoom in the regions of [O III] (left) and Hα (right) lines for the nine sources for which we could determine the redshifts. For each spectrum and each region, the upper panel shows the observed X-shooter 2D spectrum with the 1 arcsec aperture used to extract the 1D spectrum labelled. The central panel shows in black the rest frame 1D X-shooter spectrum (smoothed for plotting purposes with a binning factor of 3–11 depending on the spectrum). The flux scale has been multiplied by $(1 + z)$ in order to conserve the observed integrated flux in the rest-frame fit and is maintained the same for each source to ease the comparison of the relative strength of the emission lines. The dotted lines mark the wavelengths of Hβ, [O III] 4959, [O III] 5007 (left) and [N II] 6548, Hα, [N II] 6581, and the [S II] doublet (right), from left to right, respectively. The regions excluded from the fit below the Gaussian components and corresponding to the most intense sky lines are highlighted as shaded areas. Superimposed on the spectra are the best-fitting components presented in Section 4.2, with arbitrary normalization in order to ease the visualization: solid (blue) curves represent the systemic component ('S'); dashed (blue) curves the broad, shifted component ('B'). The solid (green) curves below Hβ and Hα with FWHM $\gtrsim$ 2000 km s^{-1} represent the very broad component ('VB'). The red solid curve shows the best-fitting sum of all components (including the power law). When only one component is needed, the fit is shown as red curve only. In the bottom panel of each fit the residuals with respect to the best fit are shown. XID 5321 and XID 2028 are shown here. Zoom in the regions of the [O III] (left) and Hα (right) for XID 5325 and XID 175. See previous page for description. Zoom in the regions of the [O III] (left) and Hα (right) for XID 18 and XID 5053. See previous page for description. Zoom in the regions of the [O III] (left) and Hα (right) for XID 60053 (first row). In the second row we show the [O III] region for XID 5573 (left) and the Hα region for 54466 (right). See previous page for description.

doublets). We imposed the following constraints: (i) the flux ratios between [O III] λ4959 and [O III] λ5007 and between [N II] λ6548 and [N II] λ6583 were fixed at 1:2.99 (Osterbrock 1981); (ii) the widths (FWHM) of the components of each line were set to be equal and <550 km s^{-1}; (iii) the relative wavelength of the lines was constrained to be equal to the laboratory differences.

Set 2: (broad, 'B'): eight Gaussian lines to model the same emission lines as detailed in Set 1 (with the same constraints described above), but with no limit to the FWHM.

Set 3: (very broad, 'VB'): two very broad (FWHM $\gtrsim$ 2000 km s^{-1}) Gaussian (or Lorentzian) functions, for the Hα and Hβ lines. For this component we only used the constraint that the
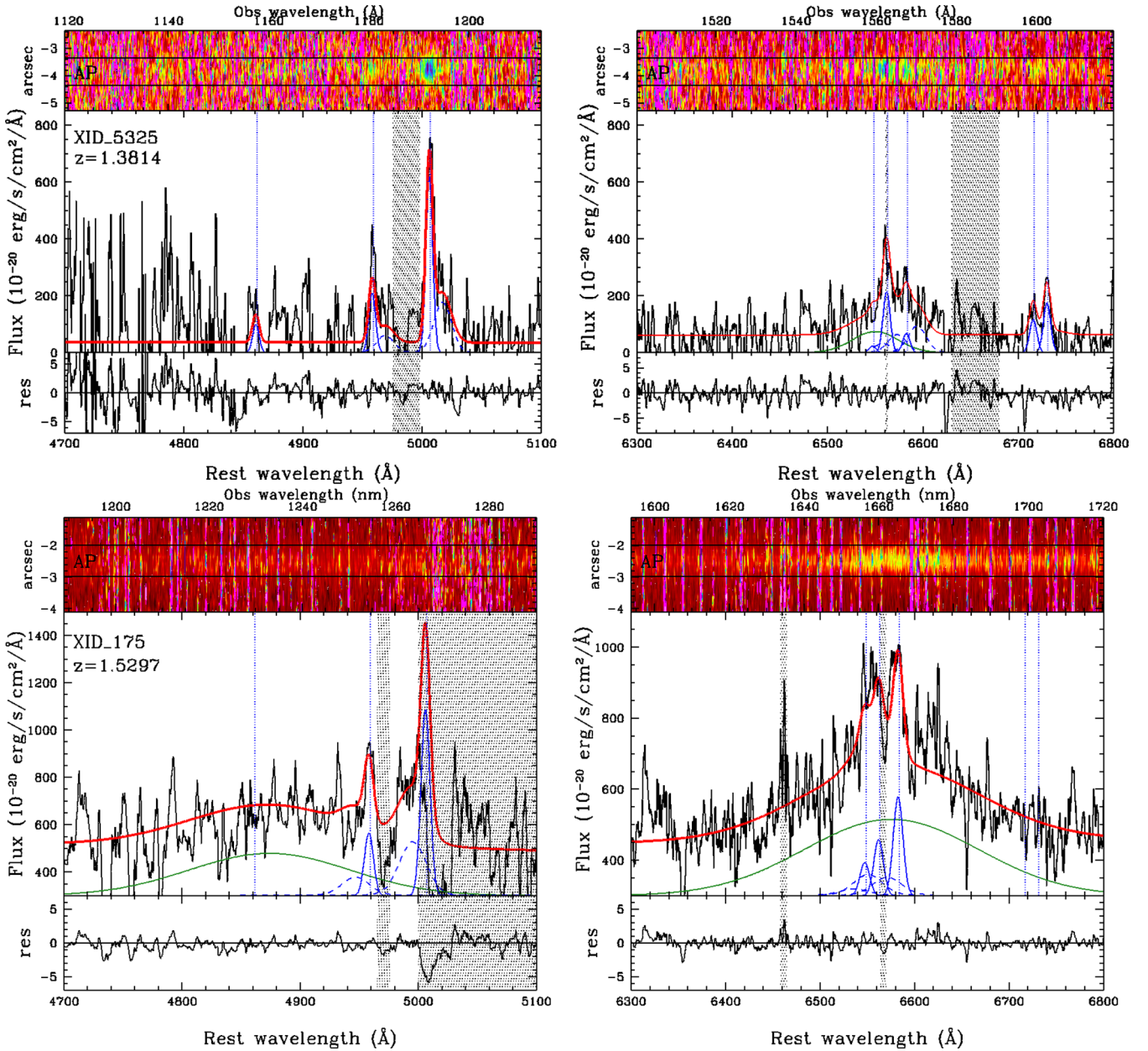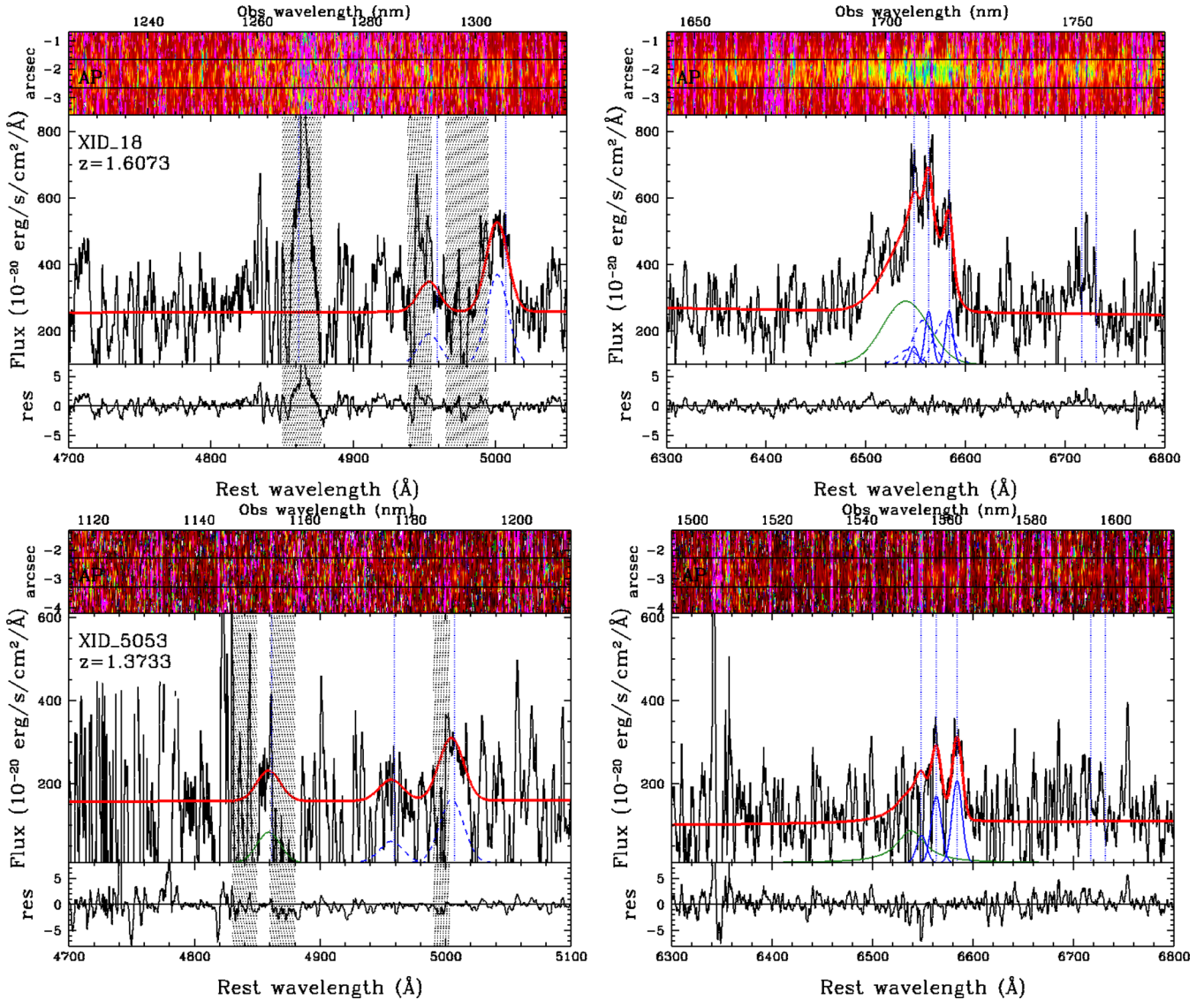
Figure 6 – *continued*

widths of Hα and Hβ are forced to be equal. This component is used only when needed/required.

From a physical point of view, the first component should trace the systemic emission of the source associated with both the narrow-line region (NLR) and SF (when present); for this reason we limit the FWHM to $\lesssim 550\,\mathrm{km\,s^{-1}}$. The second component should trace the outflowing gas. Finally, we introduced the third component to account for the possible presence of Hα and Hβ emission originated in the broad-line region (BLR).

We fit the Gaussian profiles using a FORTRAN code implementing the MINUIT package (James & Roos 1975), originally developed for high-energy physics. In the first run we fit only the prominent emission lines which have high S/N and are less affected by atmospheric features. Then, we initialize the parameters with the values obtained previously. In the fitting procedure, the χ^2 minimization

is done using as error on single fluxes the variance evaluated in the continuum ranges previously indicated. The need for the second set of lines was evaluated based both on the errors of the fits and a visual inspection of the residuals (see Section 4.3).

The best-fitting solution of the modelling described above in the region of the Hβ+[O III] is shown as a red curve in Fig. 6. The best-fitting Gaussian components needed to fit the full line profiles are also superimposed with arbitrary normalization in order to ease the visualization: the 'S' component, as solid/blue; the 'B' component as dashed/blue; the 'VB' component in solid/green. The bottom panel shows the residuals ((data-model)/error, where the error is estimated in the local continuum) that, added in quadrature, determine the χ^2. In the right-hand panel for each spectrum we also show the corresponding fits for the Hα+[N II]+[S II] region used as additional constraints on the FWHM of the [O III] lines profiles:

Figure 6 – *continued*

in particular, the 'S', 'B' and 'VB' components, when present, are fixed at the same redshift and relative shifts as those present in the left-hand panels. Table 2 summarizes the parameters obtained for the 'systemic' (S) and 'broad' (B) components for the [O III] 5007 line. The reduced minimum $\chi^2_{\rm red}$ values obtained for the proposed best-fitting solutions are reported in the last column.

Before discussing the results on the broad component associated with the outflow, we note that the FWHM and fluxes of the 'VB' component associated with the BLR are in agreement with those presented in Bongiorno et al. (2014), despite the different modelling of the narrow components, and we refer to that paper for the estimate of the BH masses. We also note that in most of the sources where a 'VB' component in the Hα region is detected, originating from the BLR (XID 5321, XID 2028, XID 18, XID 175, XID 60053 and XID 5325; see also Bongiorno et al. 2014) the Hβ is considerably extincted (with R(Hα/Hβ) $\sim$ 5–10). This is consistent with a type 1.8–1.9 nature of the objects and with the moderate obscuration measured in the X-ray spectra ($N_{\rm H} \sim 10^{21-22}$ cm^{-2}).

4.3 Incidence of broad [O III] 5007 emission lines

Four out of eight sources (XID 2028, XID 5321, XID 175 and XID 5325) need all three sets of Gaussians to reproduce simultaneously the Hβ+[O III] and Hα+[N II] line profiles. The fit with a single set of Gaussian lines to model the NLR emission, even without imposing an upper limit on the FWHM, produced a significantly larger χ^2. This is particularly true for our highest S/N sources (XID 5321 and XID 2028), where the [O III] emission is clearly asymmetric and a single component therefore cannot reproduce the observed emission (Perna et al. 2014). In all cases, the normalizations of the 'S' and 'B' Gaussians lines needed to fit the [O III] profiles were not consistent with zero (while these may be the case for other lines of the same components at lower S/N, e.g. [S II]). In four cases, the 'B' component shows a significant shift ($|\Delta v| > 300$ km s^{-1}) from the systemic redshift of the galaxy: XID 2028 and XID 175 reveal a blueshift component, while XID 5321 and XID 5325 show a redshifted component. We note that
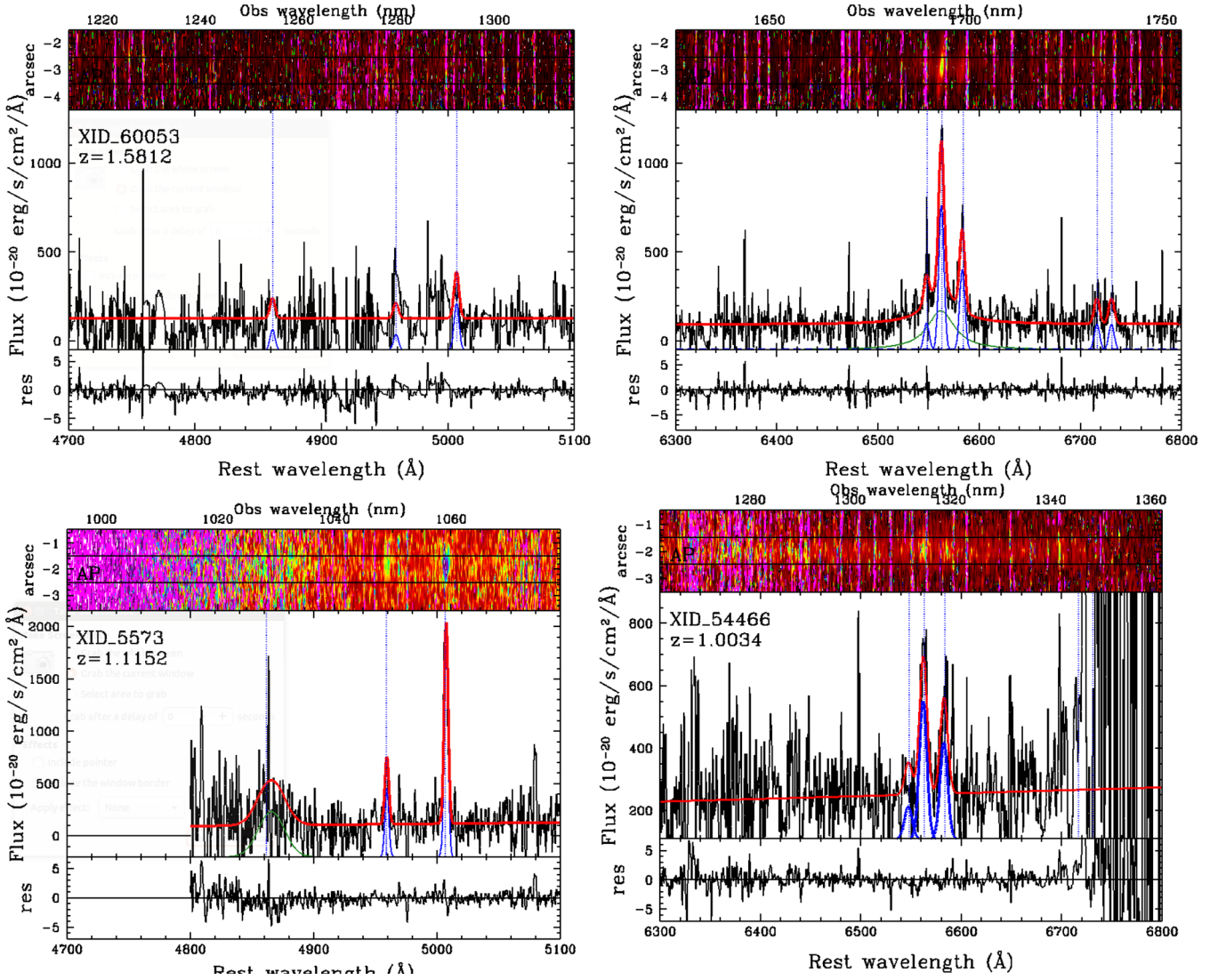
Figure 6 – *continued*

Table 2. Fit results.

XID	Specz	λ(S) (nm)	FWHM(S) (km s^{-1})	Flux(S) (10^{-20})	λ(B) (nm)	FWHM(B) (km s^{-1})	Flux(B) (10^{-20})	Δv (km s^{-1})	χ$^2_{red}$
				Fit to the [O III] 5007 line in *XMM*-COSMOS obscured QSOs					
18	1.6073	(1305.52)	(404 ± 85)	(From Hα fit)	1304.28	1065 ± 409	4883 ± 1875	−287	0.75
60053^a	1.5812	1292.35	272 ± 11	782 ± 65	–	–	–	–	0.74
175	1.5297	1266.44	513 ± 46	8167 ± 301	1263.53	1652 ± 150	7541 ± 685	−688	0.50
2028	1.5927	1298.24	520 ± 17	29188 ± 658	1296.45	913 ± 37	17127 ± 694	−413	0.99
5321	1.4702	1236.80	272 ± 14	5556 ± 149	1238.31	1306 ± 14	74664 ± 800	366	1.10
5053	1.3735	(1188.48)	(538 ± 24)	(From Hα fit)	1187.96	1372 ± 616	3655 ± 1641	−131	1.74
5325	1.3809	1191.85	403 ± 12	4448 ± 52	1194.45	1050 ± 210	3313 ± 662	653	1.76
5573	1.1152	1059.14	233 ± 10	7982 ± 93	–	–	–	–	1.02

Notes. Fluxes are in units of 10^{-20} erg cm^{-2} s^{-1}. λ(S), FWHM(S) and Flux(S) denote the best-fitting parameters and errors for the 'systemic' (S) component; λ(B), FWHM(B) and Flux(B) instead refer to the 'broad' (B) component. Δv is measured from the difference in centroids of the two measured components (B−S). Values in parenthesis refer to measurements constrained from the Hα region fit.
^{a}Two components fit not significant. Narrow component consistent with only NLs seen in the Hα region.

the velocity shift measured for the [O III] line Gaussian decomposition for XID 2028 ($\Delta v \sim -370\,\text{km s}^{-1}$) is consistent with the value reported in B10 and measured from the shift of the Mg II absorption lines in the Keck spectrum ($\Delta v \sim -300\,\text{km s}^{-1}$). A similar fraction of 'double' to 'single' line modelling has been found in H12: four out of the eight targets presented in that work needed a multiple component fit (see their fig. 3).

For the remaining four targets, in two cases (XID 18 and XID 5053) the quality of the spectra was not such to allow a 2 Gaussian decomposition below the [O III] lines and the fit has been limited to a single, blueshifted broad component,[5] whose centroid has been constrained from the combined fit on the Hα region. The detection of the broad component for these two sources is significant at the 2–3σ confidence level. For XID 5573, the best fit of the [O III] line has been obtained with only a narrow component (FWHM $\sim 230\,\text{km s}^{-1}$). Finally, for XID 60053 only narrow components are detected in the Hα region, in correspondence with two peaks observed also in the [O III] lines (as labelled in Fig. 6). The observed Hα flux, if ascribed entirely to SF, translates into a SFR $\sim 10\,\text{M}_\odot\,\text{yr}^{-1}$ (Kennicutt 1998). From the comparison of the SFR from the FIR and the Hα, we infer a lower limit to the extinction of $A_V \sim 6$ mag. Such a high extinction would also suppress most of the [O III] flux which indeed is only barely detected in the X-shooter spectrum.

Summarizing, for six out of eight targets we report the presence of broad and shifted components with FWHM in the range 900–1600 km s^{-1} (4/6 with high significance, while the remaining two at a $\sim$2–3σ confidence level), while in the remaining two sources only narrow components (FWHM $\sim 250\,\text{km s}^{-1}$) are revealed in the [O III] lines. The incidence of redshifted lines in the sample with broad components is 33 per cent (2/6).

5 THE ORIGIN OF THE BROAD COMPONENT

The detected FWHMs are far too high to be due to rotational motions in the host galaxy, for which the velocity dispersions rarely exceed 600 km s^{-1} (see e.g. discussion in Liu et al. 2013). Similarly, we rule out that the observed large and shifted velocities may be all ascribed to complex kinematics as a result of a merging system, as the deep ACS images of the sources do not show any obvious counterpart and sign of major mergers in the 1 arcsec aperture used for the extraction of the spectra (see Fig. 3).

Emission from ionized gas in the forbidden lines, like [O III], is suppressed by collisional de-excitation when produced in high-density environments. Therefore, the observed large FWHM of [O III] cannot be ascribed to the BLR (usually confined to <1 pc scale). Instead, forbidden ionized lines can be produced at scales of the NLR. Moreover, type 1 and type 2 quasars are also often associated with extended emission line regions (EELRs) which can extend sometimes for tens of kpc (e.g. Boroson, Persson & Oke 1985; Fu & Stockton 2009; Villar-Martín et al. 2011), well beyond the size of the NLR. Fu & Stockton (2009) noted that the most likely explanation for the existence of EELR in radio-loud samples is the presence of gas swept out of the host galaxy by a blast wave accompanying the production of the radio jets. Similar conclusions have been reached by Matsuoka (2012) and extended to the whole AGN population (see also Villar-Martín et al. 2011). The chosen apertures in our samples (corresponding to $R \sim 4$ kpc) contain

emission from both the NLR and, when existing, the EELR. The observed line emission may be therefore broadened by bulk flow emission likely ascribed to an outflowing wind in conditions similar to those observed in EELR (see Matsuoka 2012). In this case the large FWHM observed may be directly related to the outflow velocity and the analysis of NIR integrated spectra of AGN at $z > 1$ bring important information on the outflow properties (see e.g. Förster Schreiber et al. 2014).

Following H12, in Fig. 7 we plot as blue circles the FWHM of the broadest components ('B' or 'S' in the case of single Gaussian fits) in our measurements versus the total [O III] luminosity, and we compare them with different literature samples, both local and at high redshift. We chose to plot the total *observed* [O III] luminosity (i.e. not corrected for extinction) in order to ease the comparison with previous published works. The possible effects of reddening will be discussed when relevant and we will take this into accounts when referring to the energetic of the systems.

5.1 QSOs in star-forming/ULIRGs hosts

As mentioned in the Introduction, most previously reported studies which showed convincing evidence of the existence of large-scale outflows have been conducted on AGN–ULIRGs systems. Given the concomitant presence of on-going SF and BH activity, it is not obvious to determine which is the main driver of the observed outflowing wind. In the bottom panel of Fig. 7 we compare our results on the FWHM and integrated line flux with those obtained for QSO–ULIRGs systems, at both low and high redshift.

Rodríguez-Zaurín et al. (2013, hereafter R-Z13) showed that in a nearly complete sample of local ULIRGs, those associated *with* Seyfert nuclei show evidence of broad and shifted lines on scale of $\sim$5 kpc, while those *without* Seyfert nuclei do not show the complex and extended kinematics observed in their active siblings (see also Zakamska & Greene 2014; see similar results on striking differences in the molecular gas outflow properties of AGN ULIRGs versus non-AGN ULIRGs presented in Cicone et al. 2014). This may be seen as an indication that the presence of the AGN rather than the on-going star formation may be the major cause for the complex (extended) NLR kinematics in local ULIRGs (but see Soto et al. 2012; Soto & Martin 2012 for different results). The complex kinematic properties of the Sey–ULIRGs systems in the local Universe (with up to three or more different components needed to fit the observed [O III] profiles) emerge also in Fig. 7 (upper panel): most of the objects in the R-Z13 sample (cyan points) have FWHM $> 1000\,\text{km s}^{-1}$. The presence of outflowing ionized gas in these systems is confirmed by IFU data (see e.g. Westmoquette et al. 2012, where the fastest outflows are associated with systems that contain AGN), and by the fact that the broadest components measured in R-Z13 lie in the AGN-photoionized region in the BPT diagrams (Baldwin, Phillips & Terlevich 1981).

The red squares in the upper panel of Fig. 7 are the eight $z \sim 2$ SMG/ULIRGs with AGN signatures presented in H12, with on average FWHM $\sim 1000\,\text{km s}^{-1}$. Thanks to the availability of IFU data, the presence of large-scale outflows has been unambiguously traced up to scales of 10–20 kpc also in the majority of these systems. Similarly, Förster Schreiber et al. (2014) observed with SINFONI eight massive ($M_* > 10^{11}\,\text{M}_\odot$) star-forming galaxies at $z \sim 2$, half of them with clear AGN signatures. On the basis of spatially resolved spectral analysis of the Hα complex, they found evidence for powerful AGN-driven nuclear outflows with

---

[5] In this case the definition of 'S' and 'B' is superseded, but we report these values in the column 'B' in Table 2.
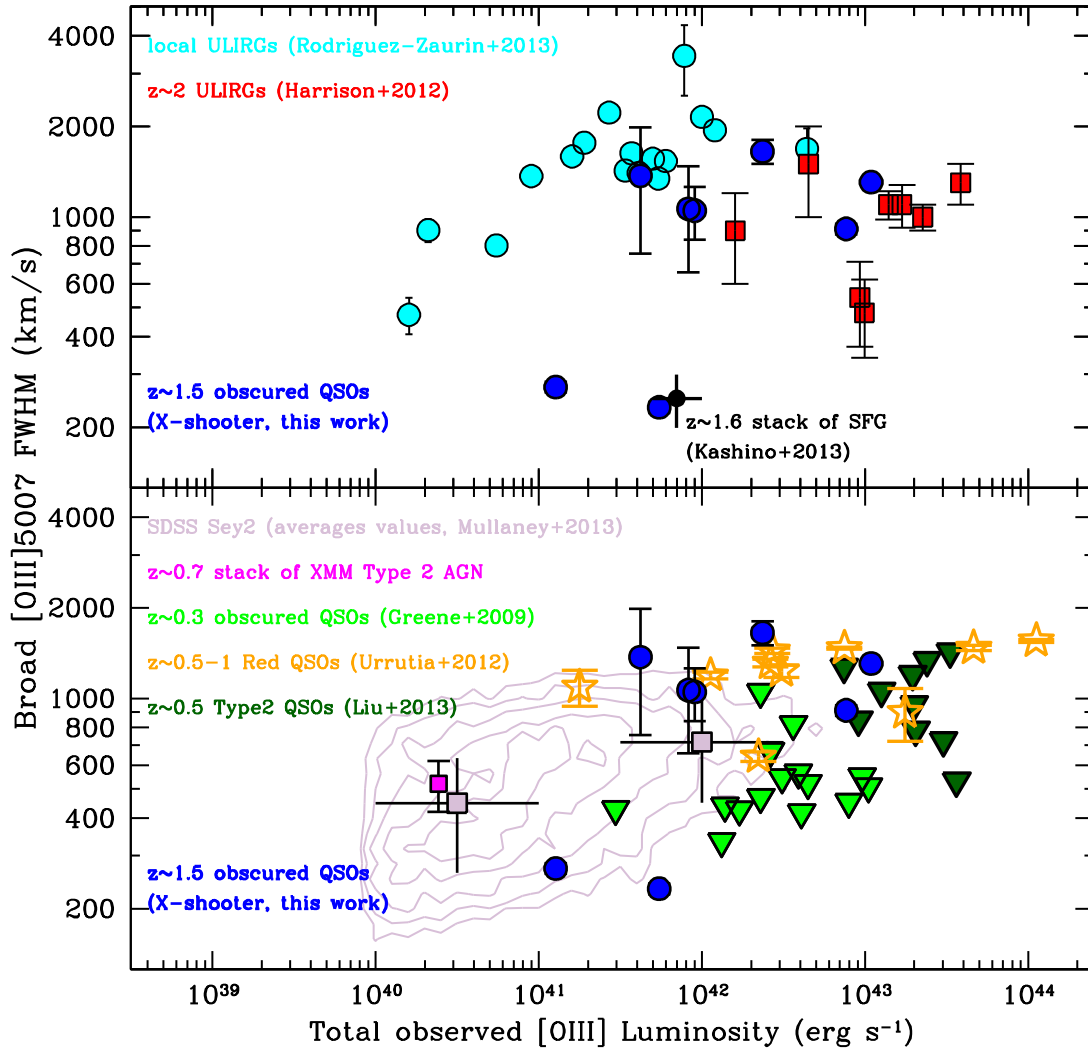
Figure 7. FWHM (broad component) of the 5007 Å line against the total [O III] 5007 luminosity. The [O III] luminosity is not corrected for extinction. In both panels our X-shooter targets are marked with blue circles. For completeness, we also plot the two sources (XID 5573 and XID 60053), fitted by only a narrow component in the [O III] lines, by using the FWHM of the 'S' component. Our results are compared with known literature samples of star-forming systems (both ULIRGs and MS; upper panel) and Sey2 and type 2 QSOs (lower panel), as labelled (see Sections 5.1 and 5.2). The black filled circle in the upper panel represents the average for a population of 30 massive star-forming galaxies at $z \sim 1.6$ (Kashino et al. 2013, see text for details). The magenta square in the lower panel represents the result from the stacked spectrum of ~110 *XMM*-COSMOS type 2 QSOs with spectra available from the zCOSMOS 20k survey in the range $z = 0.5$–0.9, without any pre-selection on their optical/IR colours. Following H12, in this plot in the case of fits with multiple Gaussian components, the FWHM from the 'B' component is plotted. Otherwise, the FWHM derived from a single component fit is adopted. For the objects in the sample of Liu et al. (2013) we use the velocity widths containing 80 per cent of the flux (W80). The [O III] luminosity is instead derived from the total [O III] flux for all samples.

FWHM $\sim 1500 \, \mathrm{km \, s^{-1}}$ out to scales of 2–3 kpc in the stacked spectrum of these massive systems.[6]

Altogether, these observational results suggest that FWHM larger than $1000 \, \mathrm{km \, s^{-1}}$ can be safely used to advocate the presence of kpc scale outflows, and that the AGN is likely the driving force. The six *XMM*-COSMOS obscured QSOs for which a broad component has been detected have FWHMs comparable to those measured in $z \sim 2$ QSO/SF systems. Different from these systems, though, as detailed in Section 2.2, our six targets have not been pre-selected on the basis of their SF properties and span a quite large range of SFR, from $\sim 500 \, \mathrm{M_\odot \, yr^{-1}}$ to basically passive systems. Overall, this

may be another indication that the AGN rather than the on-going star formation sample may be the major driver for the presence of the observed broad and shifted components.

In order to compare our results with pure star-forming systems, we plot in Fig. 7 the average FWHM (~ 4.2 Å corresponding to $\sim 250 \, \mathrm{km \, s^{-1}}$ in the velocity space) as a function of the un-corrected [O III] luminosity measured on the stacked spectrum of a sample of 30 massive ($\log M_* = 10.76$–11.35) star-forming galaxies selected to be on the MS at $z \sim 1.6$ and observed with Fiber Multi-Object Spectrograph (FMOS) in the COSMOS survey (Kashino et al. 2013, black filled circle). In this case, the stacked spectrum has been constructed by carefully excluding AGN from the sample. All our targets have measured FWHM of the broad (and shifted) component well above the average value of star-forming galaxies at the same redshift (see also Newman et al. 2012). If outflows driven

---

[6] We do not report the results of Förster Schreiber et al. (2014) because we do not have information on the [O III] flux.

from SF winds were common in MS galaxies at $z \sim 1.6$, these would translate in a broadened FWHM in the stacked spectrum, which instead is not observed.

The only source above the MS in our sample with properties comparable to the SMG/ULIRGs presented in H12 and for which we have the [O III] spectrum is XID 60053 (SFR ~ 900 M$_\odot$ yr^{-1}). This object shows only narrow ('S') components in the combined fit of the Hα and [O III] lines. The possible CT nature for this source, coupled with the other observed properties (high SFR, high extinction, irregular morphology and accretion rate at the Eddington level; see Sections 2.3 and 4.3) point towards the interpretation that XID 60053 may be caught in the 'dust-enshrouded' phase of rapid black hole growth which should occur before the feedback phase. This would naturally explain the non-detection of strong broad components (as observed in XID 5321 and XID 2028) despite the similar intrinsic AGN luminosity (see next section).

5.2 Type 2 AGN samples

We now compare our results with those reported in the literature for objects selected on the basis of a purely AGN classification.

Mullaney et al. (2013) presented the analysis from a multicomponent (allowing for the presence of a broad component) line fit of the [O III] 5007 line in the SDSS population. In the lower panel of Fig. 7 we report the contour levels extracted for the type 2 AGN only, at observed total [O III] luminosities larger than 10^{40} erg s^{-1}. The pinkish-grey squares represent the average values of the 'broad' FWHM in two luminosities ranges (L[O III] $\sim 10^{40.5}$ and $\sim 10^{42}$ erg s^{-1}). All but two of our X-shooter targets have FWHM > 716 km s^{-1}, which represents the average FWHM of the broadest component in the SDSS type 2 AGN sample at L[O III] $\sim 10^{41.5-42.5}$ erg s^{-1}. We note that objects with FWHM > 900 km s^{-1} at L[O III] $\gtrsim 10^{42}$ erg s^{-1} are rare in the SDSS sample (~ 2 per cent; see Harrison 2014) while all of our five targets with observed L[O III] larger than this luminosity threshold revealed a broad component with FWHM larger than the SDSS average. We also do not find a clear trend of the broad FWHM with the L[O III] in our sample, as already pointed out in Harrison (2014).

In order to verify the efficiency of selection criteria applied to X-ray sources in detecting objects with large FWHM, we constructed the stacked spectrum of all *XMM*-COSMOS type 2 AGN at $z = 0.5$–0.9 for which [O III] is visible in the zCOSMOS spectra and without imposing any pre-selection on their optical/IR colours (~ 110 objects). We measured the FWHM in the average spectrum and the fit is consistent with a single and symmetric line component with FWHM ~ 540 km s^{-1} (magenta square in Fig. 7). This value is consistent with the average value of the broadest component observed in the SDSS sample at comparable observed [O III] luminosities (L[O III] $= 10^{40-41}$ erg s^{-1}, FWHM ~ 450 km s^{-1}; see also Heckman et al. 1981). We note that both the SDSS type 2 and the *XMM*-COSMOS type 2 samples may contain also objects in the feedback phase (which occur at different L and redshift due to the downsizing) and therefore with individual large FWHM associated with blueshifted (or redshifted) [O III] lines, but they are washed out in the average stacking.

The higher average FWHM measured in our sample with respect to the $z \sim 0.7$ *XMM*-COSMOS type 2 AGN may be due to the larger luminosity of our sample, and may be in principle simply ascribed to the fact that more luminous systems are on average larger and therefore the NLR extends at larger radii (e.g. Netzer et al. 2004; see also Greene et al. 2011; Hainline et al. 2013; R-Z13; see also the higher average FWHM in SDSS type 2 AGN at high L[O III]).

In the lower panel of Fig. 7 we also plot the results for 15 type 2 QSOs from the SDSS studied in Greene et al. (2009, 2011), with total observed L[O III] $\gtrsim 10^{42}$ erg s^{-1} (light green triangles), therefore, more directly comparable to our targets. In this case no further selection in addition to line ratio diagnostic has been applied. Although the authors indicate outflows on scales extending from few up to 10 kpc as a possible origin for the observed broad widths, we notice that, on average, their values (average FWHM ~ 525 km s^{-1}) are consistent with those observed in the SDSS Seyfert 2 sample, and a factor of ~ 2 lower than the average observed in our sample. As a comparison we also plot the radio-quiet type 2 QSOs at L[O III] $\gtrsim 10^{43}$ erg s^{-1} (dark green triangles, from Liu et al. 2013), for which the existence of large-scale (~ 10 kpc) outflows over most of the extent of the gas-emitting region has been convincingly demonstrated via IFU spectroscopy. In this case we plot the W80 non-parametric measure of the line width (see discussion in Liu et al. 2013, section 2.3), which at a very first order can be used as representative of the FWHM of the lines. Also in this case, we found an average value of the line width comparable to that measured in our targets, despite their one order of magnitude larger observed [O III] luminosities.

Overall, the comparison of the results obtained in our sample and the other samples discussed above may be seen as an indication that the colour selection applied to our X-ray sample is effective in picking up objects with FWHM larger than the average values. Urrutia et al. (2012) presented a sample of 13 dust-reddened QSOs at $z = 0.5$–1, selected solely on the basis of a red $J - K$ colour. The intrinsic $E(B - V) \sim 0.5$ of these targets is similar to what is observed in our targets. We have analysed 11 out of 13 objects from the Urrutia et al. (2012) sample using the spectra provided by Glikman et al. (2012) and applying a model similar to that described in Section 4.2, limited only to the Hβ+[O III] region but including a proper modelling of the Fe II lines. The details of the fits and the results are reported in Appendix A, and the FWHMs associated with the broad component are shown as orange stars in the lower panel Fig. 7. In the hypothesis that the broad components can be ascribed to outflowing winds (see previous subsection), the high incidence of very broad lines in ours and the Urrutia et al. (2012) sample (13/19 have FWHM > 1000 km s^{-1}) in such dust-reddened QSOs may be an additional evidence that the blow-out phase is indeed heavily obscured, on the entire galactic scale.

We finally consider all the samples for which the bolometric luminosity has been derived in a similar way from a multiwavelength SED fitting (the H12 sample, the Urrutia et al. 2012 sample and our sample), and therefore an estimate of the *intrinsic* AGN bolometric luminosity can be obtained. In this way we remove the effect of the reddening on the [O III] luminosities. The FWHMs as a function of the intrinsic (bolometric) AGN luminosities for this combined sample of 27 objects are plotted in Fig. 8. We span a two orders of magnitude range in L(AGN) (10^{45}–10^{47} erg s^{-1}) and no clear trend between these two quantities is seen in these data. This result is at odds with the results recently presented in Zakamska & Greene (2014), where a trend of the [O III] width with the IR luminosity is seen in SDSS luminous type 2 quasars, as expected for outflows driven by the radiation pressure of the quasar (e.g. Menci et al. 2008).

6 MASS OUTFLOWS RATES AND ENERGETIC

In the previous section we have reported compelling evidences that the colour selection applied to our X-ray sample is effective in
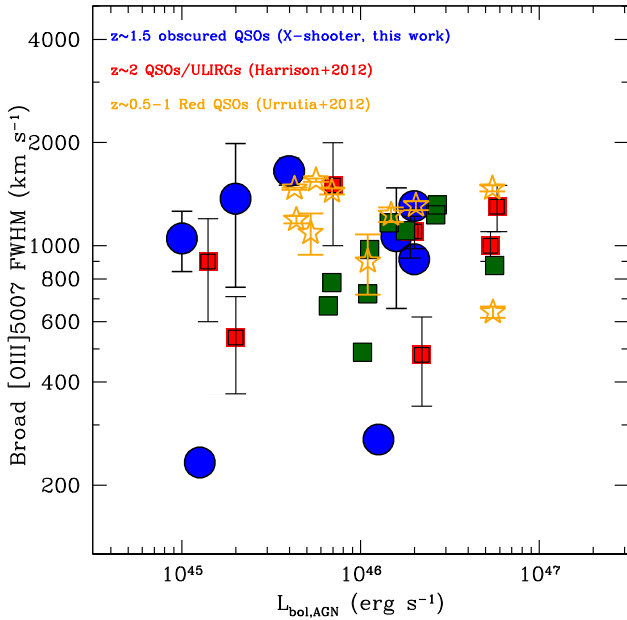
Figure 8. FWHM (broad component) of the 5007 Å line against the AGN bolometric luminosity for our targets and other two comparison samples for which AGN bolometric luminosities from SED fitting are available, as labelled (see text for details).

Table 3. Outflow kinetic powers.

XID (1)	v_{max} (2)	$\log(\dot{E}_K^{ion})$ (3)	$\log(\dot{E}_K^{tot})$ (4)
18	1230	42.20	43.20
2028	1350	42.86	43.86
175	1800	42.83	43.83
5321	1730	43.73	44.73
5053	1500	42.17	43.17
5325	1660	42.26	43.26

Notes. Column (1): XID; column (2): maximum velocity inferred from the line profile, in km s^{-1}; column (3): outflow kinetic power of the *ionized* gas component as derived from equation (1) (lower limits); column (4): inferred total outflow rates (see Section 6 for discussion). All values are in log scale, units are erg s^{-1}.

picking up objects with disturbed kinematics, which can be likely ascribed to the presence of outflowing wind. In order to unveil the mass and energy involved in the wind component, the bulk outflow velocity, the knowledge of the distribution (geometry), the density of the gas (n_e) and the spatial scale (e.g. the radius R of the emitting volume) are needed. We can derive an order of magnitude estimate of the expected outflow power under reasonable assumptions on these quantities, as detailed below.

Following the arguments presented in Cano-Díaz et al. (2012, see their appendix B), a lower limit on the kinetic power ($\dot{E}_K^{ion}$) associated with the outflows can be given by

$$\dot{E}_K^{ion} = 5.1710^{43} \frac{\mathcal{C} L_{44}([\text{O III}]) v_3^3}{\langle n_{e3} \rangle 10^{[\text{O/H}]} R_{kpc}} \text{erg s}^{-1}, \quad (1)$$

where $L_{44}([\text{O iii}])$ is the [O III] luminosity of the broad component in units of 10^{44} erg s^{-1}, n_{e3} is the electron density in units of 1000 cm^{-3}, $\mathcal{C}$ is the condensation factor (≈ 1), v_3 is the outflow velocity in units of 1000 km s^{-1}, $10^{[\text{O/H}]}$ is the metallicity in units of solar metallicity and R_{kpc} is the radius of the outflowing region, in units of kpc.

The spatial scale sampled by the extraction window (~ 1 arcsec; see upper panels in Fig. 6) corresponds to about 8 kpc at $z \sim 1.5$. Therefore, for the radius we assumed $R_{kpc} = 5$, consistent with most of the outflow measured in our data being confined in the near-nuclear region (see also R-Z13).

We can determine an estimate of the density of the outflowing gas from the ratio of the flux in the broad components of the [S II] doublet ($r = I(6717)/I(6731)$) obtained in the fit only for our highest S/N target (XID 5321). We measure a ratio of $r \sim 0.65 \pm 0.15$, which translates into 1000–3000 cm^{-3} for reasonable temperatures assumptions (Osterbrock 1989; Stanghellini & Kaler 1989). However, in the absence of a measurement for all the sources, we decided to adopt a value of $n_e = 100$ cm^{-3}, as routinely adopted in similar studies of the ionized components based on Hβ fluxes (e.g. Liu et al. 2013; Harrison et al. 2014). This choice is also justified by the

slit-resolved spectral analysis of XID 5321 presented in Perna et al. (in preparation), where we infer $n_e = 120$ cm^{-3} from the [S II] ratio at the outflow position and outside the central 1 arcsec extraction. In the equation described above, we therefore adopted for $n_{e3} = 0.1$.

Finally, for the estimate of the outflow velocity we used the maximum velocity inferred from the [O III] profile (v_{max}), which is probably representative of the average outflow velocity (see Cano-Díaz et al. 2012), as confirmed by our independent analysis on the two brightest targets based on X-shooter slit-resolved spectroscopy (Perna et al. 2014) and SINFONI data (Cresci et al., in preparation). For our targets this assumption leads to bulk velocities of the order of ~ 1200–1800 km s^{-1}. Further assuming a spherical geometry and solar metallicity, using for $v_3 = v_{max}/1000$ and computing $L[\text{O III}]$ from the integrated flux in the broad component only, we can estimate the outflow kinetic powers for our targets associated with the *ionized gas component*. The values obtained from equations (1) for our six sources with a broad components are listed in Table 3, along with the velocity measurements used in the computation of the outflow powers (v_{max}).

Admittedly, the values listed in Table 3 suffer from large uncertainties, given that the exact measurements of the densities, emissivities (depending on the temperature of the medium), metallicity and [O III] ionization status are not possible with our data. However, we are confident that the estimates obtained through equation (1) should be safely regarded as absolute lower limits to the total outflow rates, for several reasons.

First, we note that we do not correct the [O III] luminosity for the extinction and therefore we may underestimate the ionizing flux. Using the intrinsic [O III] luminosity (corrected for reddening) in equation (1) the estimate of $\dot{E}_K^{ion}$ may increase by a factor of 2–8, depending on the source.

Second, in deriving equation (1) Cano-Díaz et al. (2012) assumed that all the oxygen ions are in the O^{2+} state and that oxygen is a good tracer of the ionized gas. Hβ may provide a better tracer of the gas, given that it is independent from the assumptions on the metallicity and of the ionization state. Unfortunately, in all but our two highest S/N targets, the broad and shifted Hβ component remains undetected. In the two cases where it is detected, the Hβ flux is a factor of ~ 10 lower than the [O III] flux (see also Perna et al., in preparation). This would translate into a factor of $\gtrsim 5$–10 larger kinetic powers, when adopting routinely used calibrations from Hβ (Liu et al. 2013; Harrison et al. 2014), and depending on
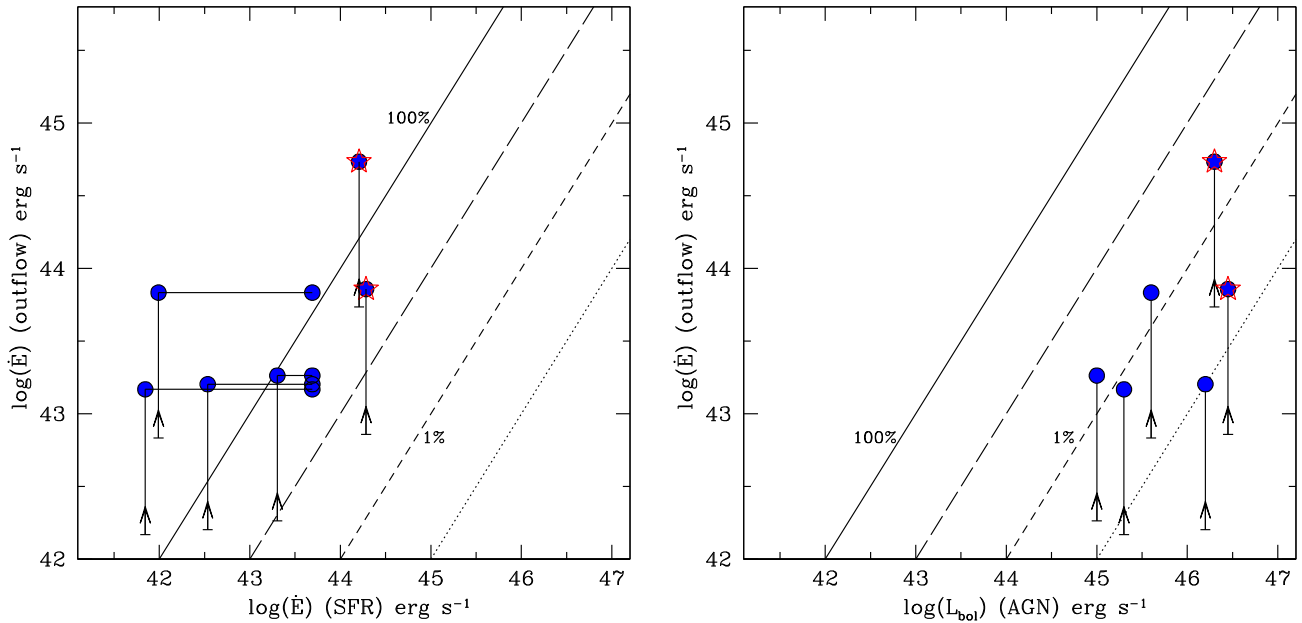
Figure 9. Left-hand panel: our inferred values of the outflow kinetic energy injection rate (i.e. last column of Table 3) against the predicted energy input rate from SF. Both quantities are derived as described in Section 6. The solid, long-dashed, dotted and short-dashed lines represent the 100 (one to one correlation), 10, 1 and 0.1 per cent ratios, respectively. Starred symbols are the sources detected in PACS (XID 2028 and XID 5321). For sources not detected by *Herschel*, the predicted energy input from SF estimated from the SFR measured from the SED fitting (left-hand symbol) and from the PACS stacked signal (right-hand symbol) are connected by a solid line. The outflow kinetic powers associated with the ionized component and derived using equation (1) are shown as lower limits (upward arrows). The value for XID 2028 (leftmost starred symbol) has been shifted in the horizontal axis by 0.15 dex for clarity in the plot. Right-hand panel: our inferred values of the outflow kinetic energy injection rate against the bolometric AGN luminosity as derived from SED multicomponent fitting (see Section 2.3). The lines and symbols have the same meaning as in the left-hand panel.

temperature assumptions. A difference of a factor of 10 is further confirmed by our spatially resolved analysis of XID 2028 based on deep SINFONI *J*-band data (Cresci et al., in preparation).

Third, and most important, the ionized wind is most likely coupled to outflowing neutral and/or molecular gas components, of the same order of magnitude of the ionized one. These additional gas components easily sum up to one order of magnitude more massive material present in the outflow, as observed in the prototype outflowing QSO Mrk 231 in the local Universe, or even more, given the typical SFR or our targets (see Harrison et al. 2014).

Following the discussion above, the total outflow rates of the sources in our sample can be reasonably inferred by applying a correction factor of 10 to the measured quantities (e.g. the lower bounds of the corrections described above). We stress again that these inferred values are only meant to be representative of the order of magnitude of the expected *total outflow power* associated with the broad components measured in our sample. These values are reported in the last column of Table 3, and are plotted in the *y*-axis of Fig. 9.

6.1 Origin of the wind

In order to investigate the possible origin of the wind, we need to compare our inferred values of the *total outflow kinetic power* with the AGN bolometric luminosities and the kinetic power expected to be ascribed to stellar processes.

The kinetic output expected from stellar processes ($\dot{E}$(SF)) has been assumed to be proportional to the SFR, and is at most $\sim 7 \times 10^{41} \times$ (SFR/M$_\odot$ yr^{-1}) following Veilleux, Cecil & Bland-Hawthorn (2005). For the AGN luminosity we use the values derived in Section 2.3.

Fig. 9 (left-hand panel) shows our inferred total outflow kinetic powers versus the predicted energy input rate from SF. Starred symbols are objects with PEP detections. For all the others, the expected $\dot{E}$(SF) assuming a SFR = 70 M$_\odot$ yr^{-1} (e.g. the value corresponding to the stacked PACS signal, see Section 2.2) is also shown (rightmost point in the *x*-axis) paired with the value obtained from the SFR derived from SED fitting (leftmost point). The right-hand panel shows instead the inferred total outflow kinetic power against the AGN bolometric luminosity. The different lines in both panels refer, from left to right to 100, 10, 1 and 0.1 per cent energy output ratios. As a comparison, in the both panels we also plot the lower limits to the outflow rate as derived from equation (1) (upward arrows; third column in Table 3) paired with the inferred total outflow powers. We notice that the uncertainties associated with the measurements of the outflow kinetic output and related to our spectral modelling (e.g. the uncertainties in the measured velocities and BL fluxes) can be neglected when compared to the much larger uncertainties coming from the systematics and assumptions discussed above.

Taking the inferred estimates of the total outflow kinetic power, from Fig. 9 (left) we see that a >50 per cent coupling between the stellar processes and the wind energy is required in order to explain the inferred energetics, corresponding to mass loading factors of 0.5 (XID 2028) to 5 (XID 5321), and up to >10 for the objects undetected by PACS. Mass loading factors close to unity or even above can be easily produced by SF-induced outflows (e.g. Martin 1999; Newman et al. 2012).

On the other hand, the AGN luminosities in our systems are largely enough to sustain the inferred outflows powers: the value of $\dot{E}$ is between 0.1 and 5 per cent of the AGN bolometric luminosity, in agreement with models which predict a reasonable coupling between the energy released by the AGN and the one needed to

drive the outflow (e.g. King 2005). An AGN origin for the outflow is indeed favoured by the high velocities observed in the winds ($>1000\,\mathrm{km\,s^{-1}}$). Such high velocities are not commonly reproduced in feedback models of 'pure' starburst galaxies (e.g. without an AGN at the centre), for which generally velocities larger than 500–$600\,\mathrm{km\,s^{-1}}$ are not expected (e.g. Murray, Quataert & Thompson 2005; Ceverino & Klypin 2009; Lagos, Lacey & Baugh 2013; but see Diamond-Stanic et al. 2012 for a different conclusion, which, however, applies only to galaxies with very high SFR surface densities). The arguments based on the wind velocity would discard a SF origin for the observed outflow even if we do not correct the power observed in the ionized gas for its associated molecular component (see similar arguments also used in Genzel et al. 2014). In addition, we note that the broad FWHMs measured in our targets undetected at 100 and 160 μm in the PEP survey provide observational evidence of the presence of such strong winds in the ionized gas component in QSOs without high SFR. Overall, this may be another indication that the AGN rather than the on-going star formation may be the major driver for the presence of the observed broad and shifted components (see also Genzel et al. 2014, for similar conclusions on lower luminosities AGN).

We finally note that an estimate of the *total* outflow kinetic power by assuming an energy conserving bubble in a uniform medium and a spherical outflow (covering factor = 1) was first proposed by Heckman, Armus & Miley (1990), and adopted in the recent past by several authors, including Harrison et al. (2012b) for their sample of $z \sim 2$ SMG galaxies to which we compare our sample. According to models of AGN feedback (e.g. King 2005), however, the assumption of an energy conservation seems to overpredict the local scaling relation and therefore would be basically discarded by local constraints.

7 CONCLUSIONS

The large body of *XMM*-COSMOS state-of-the-art multiwavelength information allowed us to devise a robust method to isolate candidate objects transitioning from being starburst dominated to AGN dominated, i.e. exactly in the phase when powerful outflows driven by the SMBH are expected. In order to study the physical properties of these systems and shed light on their origin, we obtained follow-up observations with X-shooter at VLT of 10 objects, representative of the entire population of luminous, obscured QSOs at $z \sim 1$–3 and with bolometric luminosities of $L_{\mathrm{AGN}} \sim 10^{45-46.5}\,\mathrm{erg\,s^{-1}}$. This sample is similar in size, but more homogeneous in the selection, with respect to the sample presented in H12, which represents one of the most recent analysis and study of [O III] profiles in $z \sim 2$ AGN–ULIRGs systems at similar spectral resolution ($\Delta v \sim 50\,\mathrm{km\,s^{-1}}$). Our sample also shares the same AGN bolometric luminosities of the H12 sample, and of other few additional type 2 QSO samples of similar size (10–20 objects) at $z < 1$ we used as comparison samples.

The main results of the X-shooter observations, presented in this paper, are summarized below.

(i) Thanks to its large and unique wavelength coverage, X-shooter allowed us to sample simultaneously the observed frame where emission lines are redshifted (Hα and [O III] and Hβ in the NIR spectrograph, [O II] λ3727 in the VIS spectrograph), and determine accurate redshifts from the presence of multiple emission lines for all but one of the six targets for which we had only a photometric redshift estimate, with a success rate of 80 per cent, significantly larger than what is observed in similar programs of

spectroscopic follow-up of red QSOs (see Section 4.1). Although photometric redshifts are accurate enough to define AGN samples for cosmological studies, spectroscopic confirmation is mandatory for follow-up observations to probe, in a complementary way, AGN feedback effects.

(ii) In addition to the broad components with FWHM $> 2000\,\mathrm{km\,s^{-1}}$ needed to model the Hα and Hβ emission from the BLR in the majority of our targets ('VB' components in our fits; see Bongiorno et al. 2014), we found compelling evidence for the presence of broad components in the fits of the 'narrow' line profiles of the [O III]+Hβ and Hα+[N II]+[S II] regions. In particular, four out of eight objects required two sets of Gaussians with different widths (FWHM $\lesssim 510\,\mathrm{km\,s^{-1}}$ and FWHM $\gtrsim 1000\,\mathrm{km\,s^{-1}}$) to model the six forbidden transitions ([O III], [N II] and [S II] doublets) and the associated narrow components of the Balmer lines on the scale of the NLR and likely beyond. In two of the remaining four targets for which we fit a single set of Gaussian lines we also found a best-fitting solution with a FWHM $> 1000\,\mathrm{km\,s^{-1}}$, although at a lower S/N ratio.

(iii) Thanks to the information available from the Hα line which helped us in better constraining the systemic ('S') component even in the case of low S/N data in the [O III] region, we were able to measure or infer a shift of the measured broad components in the [O III] lines from the systemic wavelengths of the order of and/or shifted $|\Delta v| \sim 300$–$700\,\mathrm{km\,s^{-1}}$; two out of six (33 per cent) of the sources for which broad components have been revealed turned out to be redshifted (see Section 4.3). H12 also reported a similar fraction of redshifted lines (25 per cent, one out of four objects in their sample with double components, see RG J0302+0010 in their fig. 3). Deep NIR spectroscopy of obscured sources can therefore start to unveil in a much unbiased way (with respect to e.g. BAL QSOs which favour only one line of sight) the ubiquitous presence of outflows in the full AGN population.

(iv) All the observed properties of the only source above the MS in our sample (XID 60053: high SFR, high extinction, no detection of broad components) coupled with the irregular morphology, an accretion rate at the Eddington level and the possible CT nature for this source (see Section 2.3) point towards the interpretation that XID 60053 may be caught in the first, still heavily obscured phase of rapid black hole growth.

(v) We compared the observed large FWHMs in our sample with literature results on pure type 2 QSOs and Seyferts (lower panel of Fig. 7) and ULIRGs/AGN systems (upper panel of Fig. 7). We found that the objects for which we detect a broad component have FWHM larger than the average value observed in SDSS type 2 AGN samples at similar observed [O III] luminosity (see pinkish-grey and green points in Fig. 7; Greene et al. 2011; Mullaney et al. 2013). This may be seen as an indication that the colour selection applied to our X-ray sample is effective in picking up objects with FWHM larger than the average values.

(vi) The similarity we observe in the integrated flux profiles and average FWHM of our targets with those derived in other samples for which the presence of kpc scales outflows likely driven by the AGN have been confirmed by IFU data (e.g. Villar-Martín et al. 2011; H12; Förster Schreiber et al. 2014; Liu et al. 2013) can be considered a clear evidence that the proposed selection does efficiently work in order to pick up objects experiencing outflowing winds.

(vii) When performing a similar analysis on a sample of $z \sim 0.5$–1 AGN at comparable bolometric luminosity as our targets and selected purely on the basis of an IR colour cut (Urrutia et al. 2012), we also found a high incidence of BLs (with FWHM $> 1000\,\mathrm{km\,s^{-1}}$).

This may be an additional evidence that the blow-out phase is indeed heavily obscured, on the entire galactic scale, as predicted in evolutionary models of AGN. This is also confirmed in our targets by their moderate to high X-ray obscuration and accretion rates (Section 2).

(viii) The main differences with respect to the previous samples at $z \sim 2$ is the *lower* starburstiness and radio luminosity of our targets: on average, our sources lie on or below the MS of star-forming galaxies at $z \sim 1.5$ while both H12 and Förster Schreiber et al. (2014) targets lie on average on the upper part or above the MS even when considering the redshift evolution of the sSFR (Karim et al. 2011; Whitaker et al. 2012).

(ix) In systems with substantial SF ongoing among our targets (SFR ~ 100–$500\,M_\odot\,\mathrm{yr}^{-1}$) the kinetic power predicted from stellar winds may in principle be enough to sustain the kinetic energy associated with the outflows, estimated under reasonable assumptions on the gas conditions (our inferred total outflows kinetic powers; see Section 6 and left-hand panel of Fig. 9). However, arguments related to the high observed winds velocities ($>1000\,\mathrm{km\,s}^{-1}$) and to the much lower coupling required to the QSO to drive the outflow (right-hand panel of Fig. 9) seem to suggest that the central luminous QSO is the most likely mechanism responsible for the launch of the wind.

8 PERSPECTIVES

Although based on observations of a small sample of sources, our X-shooter follow-up demonstrated that the adopted selection based on X-ray and optical to MIR red colours may be effective in isolating luminous obscured QSOs in the crucial 'feedback' phase predicted in galaxy–AGN co-evolution model. Large area X-ray surveys at bright X-ray fluxes with associated moderate depth multiwavelength follow-up in the IR bands, such as XXL (Pierre 2012) and Stripe-82 (LaMassa et al. 2013) can be exploited to collect larger samples of such rare objects at comparable AGN luminosities. The forthcoming eROSITA survey (Merloni et al. 2012) instead will sample the brightest end of the AGN bolometric luminosity and will yield samples of few thousands X-ray obscured QSOs at $z \sim 1$–3 and at $L_X > 10^{45}\,\mathrm{erg\,s}^{-1}$. These very powerful systems, still basically unexplored, will be those objects in which the outflows will be routinely discovered and could be studied with unprecedented details.

Although integrated NIR spectroscopy can be very powerful in detecting the presence of outflows and getting order of magnitudes estimates of the involved kinetic power, slit resolved spectroscopy and the study of the spatial distribution and intensity of the velocity field over the largest possible field of view [obtained through IFU observations such as SINFONI or *K*-band Multi-Object Spectrograph (KMOS)] will be critical in assessing the true energetics associated with the outflows and the corresponding spatial scales. IFU spectroscopy may also be critical to map the spatial distribution of the SFR (as traced by the narrow component of Hα) and verify if SF is heavily suppressed in the region with the strongest velocity component (as done in e.g. Cano-Díaz et al. 2012). This can provide a direct observational proof of quasar feedback quenching SF at high-z, measured for the first time on radio-quiet, X-ray selected obscured QSOs, more representative of the full AGN population than radio-loud and/or very luminous unobscured QSOs.

Finally, finding lower gas mass reservoirs in objects in the 'blow-out' phase, such as those presented in this work, than that measured in normal star-forming galaxies at the same redshift (e.g. Tacconi et al. 2013) would constitute another way to assess the effect of AGN feedback in diminishing the cold gas mass in the hosts galax-

ies of these 'transition' objects and will give unique insights on the time-scale of the gas consumption rate and the effect of AGN feedback in stopping SF. These can be achieved with follow-up observations with ALMA, PdBI/NOEMA and JVLA observations of CO transitions (see e.g. Feruglio et al. 2014).

REFERENCES

Alexander D. M., Hickox R. C., 2012, New Astron. Rev., 56, 93
Alexander D. M., Smail I., Bauer F. E., Chapman S. C., Blain A. W., Brandt W. N., Ivison R. J., 2005, Nature, 434, 738
Alexander D. M., Swinbank A. M., Smail I., McDermid R., Nesvadba N. P. H., 2010, MNRAS, 402, 2211
Allen J. T., Hewett P. C., Maddox N., Richards G. T., Belokurov V., 2011, MNRAS, 410, 860
Arav N., Borguet B., Chamberlain C., Edmonds D., Danforth C., 2013, MNRAS, 436, 3286
Baldwin J. A., Phillips M. M., Terlevich R., 1981, PASP, 93, 5
Banerji M., McMahon R. G., Hewett P. C., Alaghband-Zadeh S., Gonzalez-Solares E., Venemans B. P., Hawthorn M. J., 2012, MNRAS, 427, 2275
Banerji M., Fabian A. C., McMahon R. G., 2014, MNRAS, 439, 51
Bongiorno A. et al., 2012, MNRAS, 427, 3103
Bongiorno A. et al., 2014, MNRAS, 443, 2077
Borguet B. C. J., Arav N., Edmonds D., Chamberlain C., Benn C., 2013, ApJ, 762, 49
Boroson T. A., Persson S. E., Oke J. B., 1985, ApJ, 293, 120
Bournaud F., Dekel A., Teyssier R., Cacciato M., Daddi E., Juneau S., Shankar F., 2011, ApJ, 741, L33
Brusa M. et al., 2005, A&A, 432, 69
Brusa M. et al., 2010, ApJ, 716, 348 (B10)
Cano-Díaz M., Maiolino R., Marconi A., Netzer H., Shemmer O., Cresci G., 2012, A&A, 537, L8
Cappelluti N. et al., 2009, A&A, 497, 635

Cen R., 2012, ApJ, 755, 28

Ceverino D., Klypin A., 2009, ApJ, 695, 292

Cicone C. et al., 2014, A&A, 562, A21

Ciotti L., Ostriker J. P., 2007, ApJ, 665, 1038

Dai X., Shankar F., Sivakoff G. R., 2008, ApJ, 672, 108

Dale D. A., Helou G., 2002, ApJ, 576, 159

de Kool M., Arav N., Becker R. H., Gregg M. D., White R. L., Laurent-Muehleisen S. A., Price T., Korista K. T., 2001, ApJ, 548, 609

Diamond-Stanic A. M., Moustakas J., Tremonti C. A., Coil A. L., Hickox R. C., Robaina A. R., Rudnick G. H., Sell P. H., 2012, ApJ, 755, L26

D'Odorico S. et al., 2006, Proc. SPIE, 6269, 626933

Dunn J. P. et al., 2010, ApJ, 709, 611

Elvis M., 2000, ApJ, 545, 63

Eracleous M., Halpern J. P., 1994, ApJS, 90, 1

Fabian A. C., 2012, ARA&A, 50, 455

Ferrarese L., Merritt D., 2000, ApJ, 539, L9

Feruglio C., Maiolino R., Piconcelli E., Menci N., Aussel H., Lamastra A., Fiore F., 2010, A&A, 518, L155

Feruglio C. et al., 2014, A&A, 535, 91

Fiore F. et al., 2003, A&A, 409, 79

Fiore F. et al., 2009, ApJ, 693, 447

Fischer J. et al., 2010, A&A, 518, L41

Förster Schreiber N. M. et al., 2014, ApJ, 787, 38

Freudling W., Romaniello M., Bramich D. M., Ballester P., Forchi V., García-Dabló C. E., Moehler S., Neeser M. J., 2013, A&A, 559, A96

Fu H., Stockton A., 2009, ApJ, 690, 953

Gebhardt K. et al., 2000, ApJ, 539, L13

Genzel R. et al., 2014, ApJ, 796, 7

Gindilis L. M., Pariiskii N. N., 1961, SvA, 5, 72

Glikman E. et al., 2012, ApJ, 757, 51

Greene J. E., Zakamska N. L., Liu X., Barth A. J., Ho L. C., 2009, ApJ, 702, 441

Greene J. E., Zakamska N. L., Ho L. C., Barth A. J., 2011, ApJ, 732, 9

Gültekin K., Cackett E. M., Miller J. M., Di Matteo T., Markoff S., Richstone D. O., 2009, ApJ, 706, 404

Hainline K. N., Hickox R., Greene J. E., Myers A. D., Zakamska N. L., 2013, ApJ, 774, 145

Hamann F., Korista K. T., Ferland G. J., Warner C., Baldwin J., 2002, ApJ, 564, 592

Harrison C. M., 2014, Proc. IAU Symp. 304, Multiwavelength AGN Surveys and Studies. p. 284

Harrison C. M. et al., 2012a, ApJ, 760, L15

Harrison C. M. et al., 2012b, MNRAS, 426, 1073 (H12)

Harrison C. M., Alexander D. M., Mullaney J. R., Swinbank A. M., 2014, MNRAS, 441, 3306

Hasinger G. et al., 2007, ApJS, 172, 29

Heckman T. M., Miley G. K., van Breugel W. J. M., Butcher H. R., 1981, ApJ, 247, 403

Heckman T. M., Armus L., Miley G. K., 1990, ApJS, 74, 833

Hickox R. C., Mullaney J. R., Alexander D. M., Chen C.-T. J., Civano F. M., Goulding A. D., Hainline K. N., 2014, ApJ, 782, 9

Hopkins P. F., Hernquist L., Cox T. J., Kereš D., 2008, ApJS, 175, 356

James F., Roos M., 1975, Comput. Phys. Commun., 10, 343

Karim A. et al., 2011, ApJ, 730, 61

Kashino D. et al., 2013, ApJ, 777, L8

Kennicutt R. C., Jr, 1998, ARA&A, 36, 189

King A., 2005, ApJ, 635, L121

King A., 2010, in Maraschi L., Ghisellini G., Ceca R. D., Tavecchio F., Accretion and Ejection in AGN: a Global View. Proceedings of a conference held June 22-26, 2009 in Como, Italy, p. 315

Kovačević J., Popović L. Č., Dimitrijević M. S., 2010, ApJS, 189, 15

Lagos C. d. P., Lacey C. G., Baugh C. M., 2013, MNRAS, 436, 1787

LaMassa S. M. et al., 2013, MNRAS, 436, 3581

Lamastra A., Menci N., Fiore F., Santini P., Bongiorno A., Piconcelli E., 2013, A&A, 559, A56

Lípari S. L., Terlevich R. J., 2006, MNRAS, 368, 1001

Liu G., Zakamska N. L., Greene J. E., Nesvadba N. P. H., Liu X., 2013, MNRAS, 436, 2576

Liu G., Zakamska N. L., Greene J. E., 2014, MNRAS, 442, 1303

Lusso E. et al., 2012, MNRAS, 425, 623

Lusso E. et al., 2013, ApJ, 777, 86

Lutz D. et al., 2011, A&A, 532, A90

Magorrian J. et al., 1998, AJ, 115, 2285

Mainieri V. et al., 2011, A&A, 535, A80

Maiolino R. et al., 2012, MNRAS, 425, L66

Martin C. L., 1999, ApJ, 513, 156

Martínez-Sansigre A., Rawlings S., Lacy M., Fadda D., Jarvis M. J., Marleau F. R., Simpson C., Willott C. J., 2006, MNRAS, 370, 1479

Matsuoka Y., 2012, ApJ, 750, 54

McElroy R., Croom S. M., Pracy M., Sharp R., Ho I.-T., Medling A. M., 2014, MNRAS, preprint (arXiv:1410.6552)

Menci N., Fiore F., Puccetti S., Cavaliere A., 2008, ApJ, 686, 219

Merloni A. et al., 2012, eROSITA Science Book, preprint (arXiv:1209.3114)

Merloni A. et al., 2014, MNRAS, 437, 3550

Mignoli M. et al., 2004, A&A, 418, 827

Moe M., Arav N., Bautista M. A., Korista K. T., 2009, ApJ, 706, 525

Mullaney J. R. et al., 2012, MNRAS, 419, 95

Mullaney J. R., Alexander D. M., Fine S., Goulding A. D., Harrison C. M., Hickox R. C., 2013, MNRAS, 433, 622

Murray N., Quataert E., Thompson T. A., 2005, ApJ, 618, 569

Nesvadba N. P. H., Lehnert M. D., De Breuck C., Gilbert A. M., van Breugel W., 2008, A&A, 491, 407

Nesvadba N. P. H., De Breuck C., Lehnert M. D., Best P. N., Binette L., Proga D., 2011, A&A, 525, A43

Netzer H., Shemmer O., Maiolino R., Oliva E., Croom S., Corbett E., di Fabrizio L., 2004, ApJ, 614, 558

Newman S. F. et al., 2012, ApJ, 752, 111

Osterbrock D. E., 1981, ApJ, 249, 462

Osterbrock D. E., 1989, Astrophysics of gaseous nebulae and active galactic nuclei. Research supported by the University of California, John Simon Guggenheim Memorial Foundation, University of Minnesota, et al. Mill Valley, CA, University Science Books, 1989, p. 422

Page M. J. et al., 2012, Nature, 485, 213

Pierre M., 2012, in Science from the Next Generation Imaging and Spectroscopic Surveys. ESO-Munich, Germany

Perna M. et al., 2014, A&A, preprint (arXiv:1410.5468)

Rodríguez-Zaurín J., Tadhunter C. N., Rose M., Holt J., 2013, MNRAS, 432, 138 (R-Z13)

Rosario D. J. et al., 2012, A&A, 545, 45

Rousselot P., Lidman C., Cuby J.-G., Moreels G., Monnet G., 2000, A&A, 354, 1134

Rupke D. S. N., Veilleux S., 2011, ApJ, 729, L27

Rupke D. S. N., Veilleux S., 2013, ApJ, 775, L15

Salvato M. et al., 2011, ApJ, 742, 61

Sanders D. B., Soifer B. T., Elias J. H., Neugebauer G., Matthews K., 1988, ApJ, 328, L35

Santini P. et al., 2009, A&A, 504, 751

Santini P. et al., 2012, A&A, 540, A109

Sarria J. E., Maiolino R., La Franca F., Pozzi F., Fiore F., Marconi A., Vignali C., Comastri A., 2010, A&A, 522, L3

Schinnerer E. et al., 2010, ApJS, 188, 384

Scoville N. et al., 2007, ApJS, 172, 1

Soltan A., 1982, MNRAS, 200, 115

Soto K. T., Martin C. L., 2012, ApJS, 203, 3

Soto K. T., Martin C. L., Prescott M. K. M., Armus L., 2012, ApJ, 757, 86

Spergel D. N. et al., 2003, ApJS, 148, 175

Stanghellini L., Kaler J. B., 1989, ApJ, 343, 811

Tacconi L. J. et al., 2013, ApJ, 768, 74

Urrutia T., Lacy M., Becker R. H., 2008, ApJ, 674, 80

Urrutia T., Becker R. H., White R. L., Glikman E., Lacy M., Hodge J., Gregg M. D., 2009, ApJ, 698, 1095

Urrutia T., Lacy M., Spoon H., Glikman E., Petric A., Schulz B., 2012, ApJ, 757, 125

Veilleux S., Cecil G., Bland-Hawthorn J., 2005, ARA&A, 43, 769

Vernet J. et al., 2011, A&A, 536, A105

Villar-Martín M., Humphrey A., Delgado R. G., Colina L., Arribas S., 2011, MNRAS, 418, 2032

Weedman D., Sargsyan L., Lebouteiller V., Houck J., Barry D., 2012, ApJ, 761, 184

Westmoquette M. S., Clements D. L., Bendo G. J., Khan S. A., 2012, MNRAS, 424, 416

Whitaker K. E., van Dokkum P. G., Brammer G., Franx M., 2012, ApJ, 754, L29

Zakamska N. L., Greene J. E., 2014, MNRAS, 442, 784

Zhang K., Dong X.-B., Wang T.-G., Gaskell C. M., 2011, ApJ, 737, 71

APPENDIX A: FIT TO THE URRUTIA ET AL. (2012) SAMPLE

In Figure A1 we report the fit to 11 out of 13 objects in the Urrutia et al. (2012) sample. F2M 0729+3336 has low S/N, while F2M 0825+4726 has double peaked BLs, that is thought to be due to a disc-like BLR seen edge on (Eracleous & Halpern 1994), but the spectrum does not show very broad Hβ and Hα lines, or could also be from two separate AGN close to merger. However,
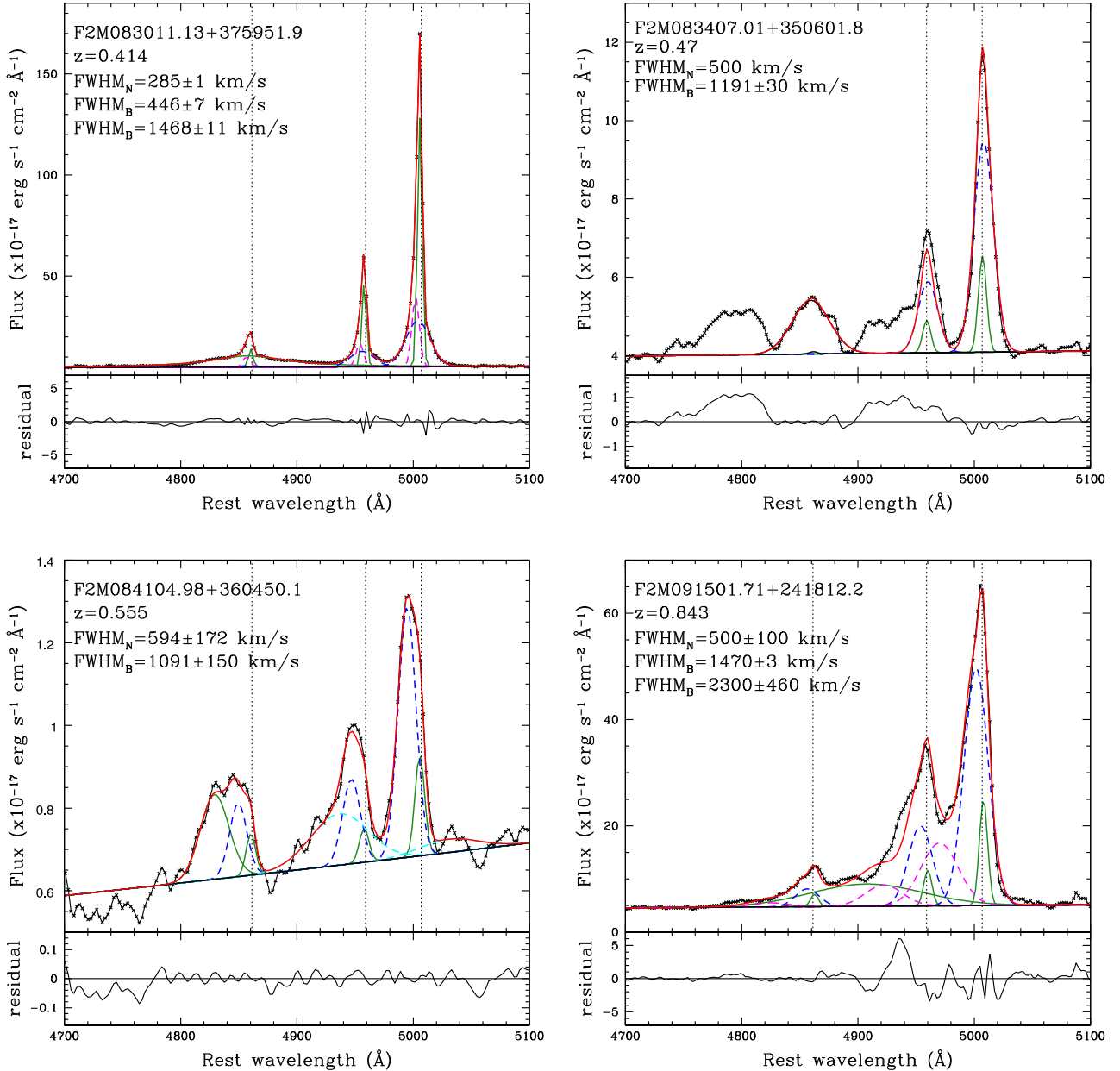

Figure A1. Fits to the Hβ + [O iii] emission lines profile of all the 12 objects in the Urrutia et al. (2012) sample, with the exception of F2M 0729+3336 (low S/N). Solid (green) curves represent the systemic component, dashed blue, magenta and gold curves the broad, shifted components. The red solid curve shows the sum of all components, and the best fit to the data. In the bottom panel of each fit the residual (differences between data and model) with respect to the best fit are shown. In cases where the lines are blended with prominent broad permitted Fe ii emission lines (F2M 0841+3604, F2M 1113+1244, F2M 1118−0033), dashed cyan curves displayed represent the fitted Fe ii components.
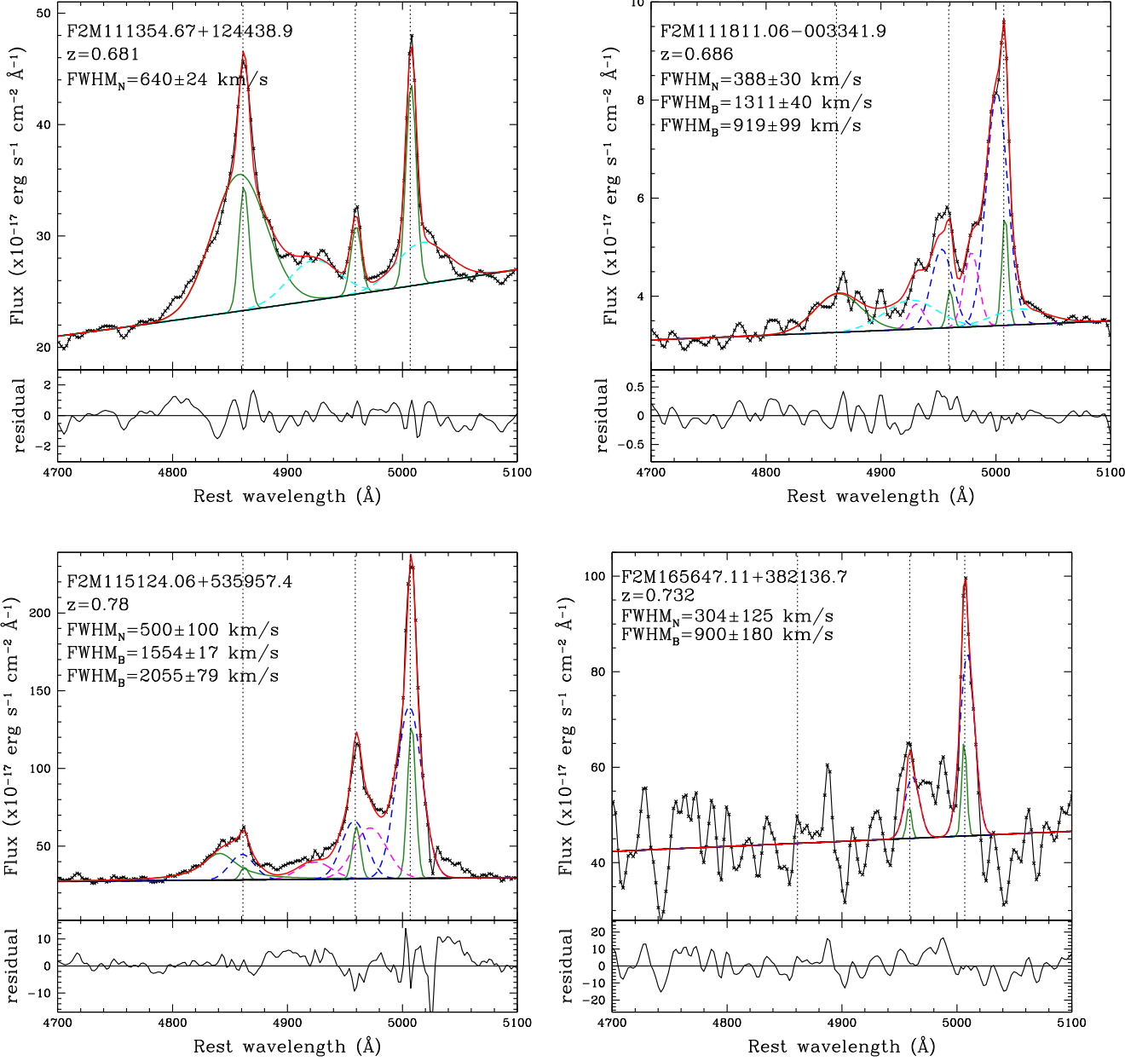
Figure A1 *– continued*

HST/ACS image does not show multiple nuclei (Urrutia, Lacy & Becker 2008). These two objects are not included in the analysis.

The model is the same as described in Section 4.2, but limited to the [O III] lines. In this case we fixed the redshift at the value given in the Urrutia et al. (2012) paper. Therefore, the rest-frame wavelength reported in Table A1 with respect to the 'S' component may be different from the rest-frame wavelength of the [O III] 5007 line. Given the better S/N in these spectra, the minimum number of Gaussian components required to fit [O III] $\lambda\lambda 4959, 5007$ emission lines ranges from one to four, with four objects (44 per cent) requiring three, three objects (33 per cent) re-

quiring two, two objects requiring one (F2M 11135+1244) and four (F2M 0825+4716) components for an adequate fit. In cases where Hβ and [O III] $\lambda\lambda 4959, 5007$ are blended with broad permitted Fe II emission lines (indicative of the presence of these, may be the blue [$\lambda\lambda 4400$–4700 Å] and red [$\lambda\lambda 5150$–5400 Å] bumps of the Fe II multiplets F, S and G in the spectra as indicated by Kovačević et al. 2010) the Fe II emission was fitted. Since all Fe II lines probably originate in the same region, with same kinematical properties, values of the relative shift and FWHM are the same for the Fe II lines; intensities are assumed to be different (Kovačević et al. 2010).
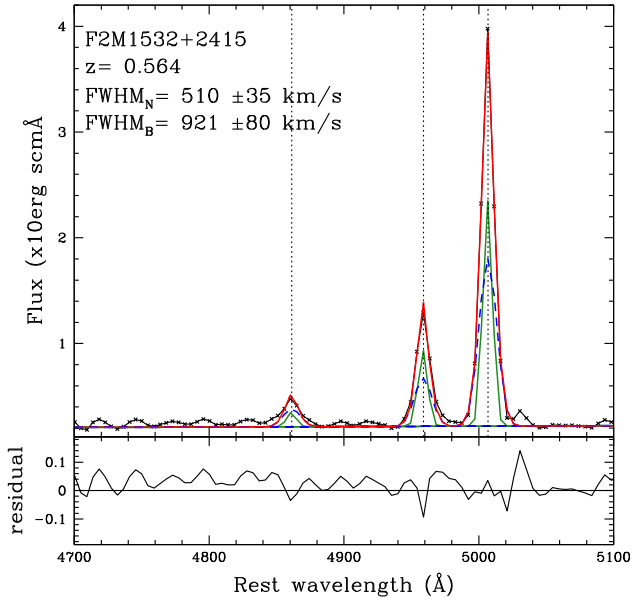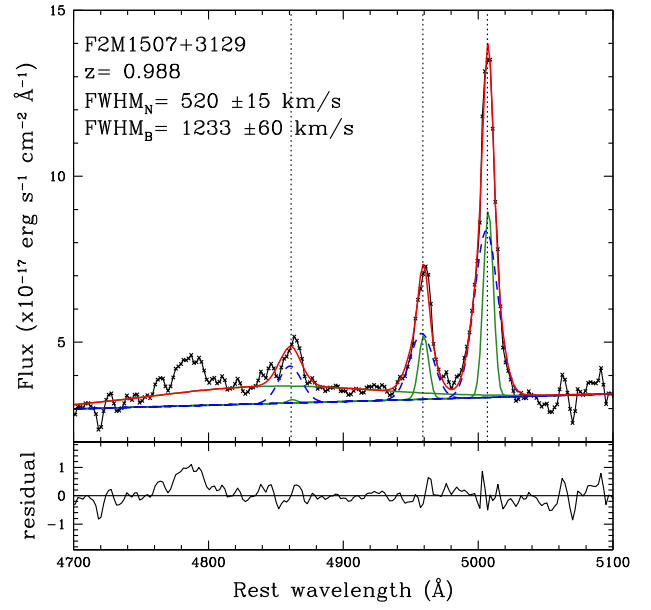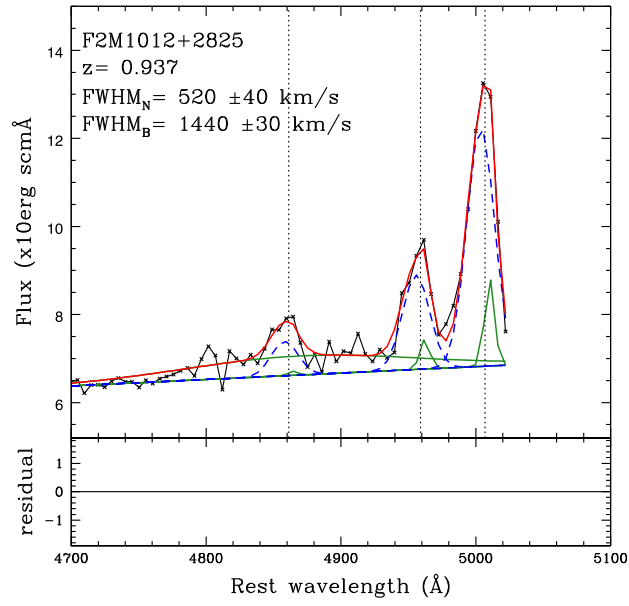
Figure A1 *– continued*

Table A1. Fit results of the Urrutia et al. (2012) sample.

ID	Specz	λ(S) (Å)	Flux(S) (10⁻¹⁷)	FWHM(S) (km s⁻¹)	λ(B) (Å)	Flux(B) (10⁻¹⁷)	FWHM(B) (km s⁻¹)	Δv (km s⁻¹)
083011+37*	0.414	5005.7 ± 0.1	624 ± 3	285 ± 2	5003.9 ± 0.1	592 ± 2	1468 ± 11	-110
083413+35	0.470	5007.1 ± 0.2	22 ± 1	500 ± 100	5007.9 ± 0.1	114 ± 1	1191 ± 30	50
084104+36	0.555	5012.1 ± 1.2	2.6 ± 0.7	594 ± 172	5001.1 ± 1.6	11.8 ± 0.7	1091 ± 150	-650
091501+24*	0.843	5010.7 ± 0.1	178 ± 1	500 ± 100	5004.4 ± 0.1	1170 ± 1	1470 ± 3	-380
111354+12	0.681	5007.6 ± 0.1	208 ± 3	640 ± 24	...	...	...	...
111811-00*	0.686	5008.0 ± 0.2	16 ± 1	388 ± 30	5000.9 ± 0.4	111 ± 1	1311 ± 40	-420
115152+53*	0.780	5008.0 ± 0.1	884 ± 6	500 ± 100	5006.0 ± 0.1	3060 ± 11	1554 ± 17	-140
165647+38	0.732	5006.3 ± 0.7	111 ± 27	304 ± 125	5009.1 ± 1.2	614 ± 33	900 ± 180	170
1012+2825	0.937	5010.2 ± 0.3	6.2 ± 0.4	520 ± 40	5003.6 ± 0.2	54.4 ± 1.5	1440 ± 30	-156
1507+3129	0.988	5007.5 ± 0.2	17.5 ± 1.4	520 ± 15	5005.9 ± 0.3	43 ± 3	1233 ± 60	-96
1532+2415	0.564	5006.4 ± 0.1	6.5 ± 1.8	510 ± 35	5006.7 ± 0.2	921 ± 80	7.4 ± 1.8	18

Notes. Fluxes are in units of 10^{-17} erg cm^{-2} s^{-1}. Wavelengths are given in the rest frame. λ(S), FWHM(S) and Flux(S) denote the best-fitting parameters and errors for the 'systemic' (narrow) component; λ(B), FWHM(B) and Flux(B) instead refer to the 'broad' (shifted) component. Objects marked with * required additional components for the line fit (see text for details and Fig. A1). In this case we report the component we most likely associate to an outflow. Δv is measured from the difference in centroids of the two measured components.

This paper has been typeset from a TEX/LATEX file prepared by the author.